

Constructing accurate and efficient general-purpose atomistic machine learning model with transferable accuracy for quantum chemistry

Yicheng Chen,^{†,¶} Wenjie Yan,^{†,¶} Zhanfeng Wang,[†] Jianming Wu,^{*,†} and Xin
Xu^{*,†,‡}

[†]*Department of Chemistry, Collaborative Innovation Center of Chemistry for Energy
Materials, Shanghai Key Laboratory of Molecular Catalysis and Innovative Materials, MOE
Key Laboratory of Computational Physical Sciences, Fudan University, 200433, Shanghai,
People's Republic of China*

[‡]*Hefei National Laboratory, 230088, Hefei, People's Republic of China*

[¶]*These authors contribute equally.*

E-mail: jianmingwu@fudan.edu.cn; xxchem@fudan.edu.cn

Abstract

Density Functional Theory (DFT) has been a cornerstone in computational science, providing powerful insights into structure-property relationships for molecules and materials through first-principles quantum-mechanical (QM) calculations. However, the advent of atomistic machine learning (ML) is reshaping the landscape by enabling large-scale dynamics simulations and high-throughput screening at DFT-equivalent accuracy with drastically reduced computational cost. Yet, the development of general-purpose atomistic ML models as surrogates for QM calculations faces several challenges, particularly in terms of model capacity, data efficiency, and transferability across

chemically diverse systems. This work introduces a novel extension of the polarizable atom interaction neural network (namely, XPaiNN) to address these challenges. Two distinct training strategies have been employed, one direct-learning and the other Δ -ML on top of a semi-empirical QM method. These methodologies have been implemented within the same framework, allowing for a detailed comparison of their results. The XPaiNN models, in particular the one using Δ -ML, not only demonstrate competitive performance on standard benchmarks, but also demonstrate the effectiveness against other ML models and QM methods on comprehensive downstream tasks, including non-covalent interactions, reaction energetics, barrier heights, geometry optimization and reaction thermodynamics, etc. This work represents a significant step forward in the pursuit of accurate and efficient atomistic ML models of general-purpose, capable of handling complex chemical systems with transferable accuracy.

Introduction

Density Functional Theory (DFT),^{1,2} stands out as an outstanding representative of modern electronic structure methods, being indispensable across various scientific disciplines over the past decades, owing to its predictive power in elucidating and predicting structure-property relationships of molecules and materials through quantum-mechanical (QM) calculations at the atomic level.³ However, the emergence of atomistic machine learning (ML) approaches^{4,5} is transforming the research paradigm. These atomistic ML models directly map geometric inputs of molecules or materials to the respective target properties, enabling large-scale dynamics simulations⁶ and high-throughput screening⁷ with accuracy comparable to those of DFT calculations, all while bypassing the traditionally intensive and costly routines of DFT calculations. Once these models are trained on datasets encompassing the relevant chemical space for the systems of interest, they significantly enhance efficiency and predictive power.

Despite the successes that have already been achieved, developing generally applicable

atomistic ML models as surrogates for QM calculations remains a significant challenge.⁸ Specifically, model capacity and data efficiency are the major concerns. A lower capacity model is unable to learn and capture complex relationships or patterns within the data, whereas a higher capacity model may perform exceptionally well on the training data but poorly on unseen or test data. As accessing vast quantities of high-quality data for achieving comprehensive coverage of all chemical space is inherently constrained, data efficiency is crucial for reducing the dependence on large annotated datasets and for developing ML models with high transferable accuracy. Furthermore, in practical applications, chemists are more interested in relative energy changes that occur during dynamic processes or chemical reactions, as opposed to mere deviations observed in static systems. This highlights a clear disparity between methodological advancements and practical needs, where the models’ ability to generalize from their training samples to chemically distinct systems, especially in downstream tasks involving relative energetics, is notably problematic.⁵

Both Deep Neural Networks (DNNs)⁹⁻¹² and Graph Neural Networks (GNNs)¹³⁻¹⁵ have been utilized in constructing atomistic ML models, aiming as general alternatives for routine computational tasks in quantum chemistry. Currently, AIQM1¹² and OrbNet-Equi¹⁵ represent the state-of-the-art (SOTA) for two types of networks, without or with, respectively, integrating electronic structure information within the NN framework. Despite their remarkable performances, there remains room for improvement in their general applicability at this stage, primarily due to architectural limitations of the models. For instance, AIQM1 is limited to systems made solely from C, H, N, and O atoms; whereas obtaining higher-order analytical gradients with OrbNet-Equi is not straightforward.¹⁶

In this work, we propose a novel design of equivariant GNN, aiming to construct an accurate and efficient atomistic ML framework for broad applicability. We dub this model XPaiNN, which architecturally extends the successful *Polarizable Atom Interaction Neural Network* (PaiNN).¹⁷ Comprehensive details regarding the model framework are presented in the **Methods** section and the **Supporting Information (SI)**. XPaiNN has demonstrated

competitive performance alongside the existing ML models on standard benchmark dataset of QM9,¹⁸ indicative of its model capacity to cover a wide chemical space. Furthermore, we have trained XPaiNN using the SPICE dataset,¹⁹ containing one million conformers across ten different element types, to establish NN potential energy models that are generally useful for organic molecules. Two distinct training methodologies have been employed, one direct-learning and the other Δ -ML on top of a semi-empirical QM (SQM) method, yielding two models that have been compared in detail against other ML models and QM methods in downstream applications. These tasks include energy benchmarks for reactions, assessments of non-covalent interactions (NCIs), conformational analyses, barrier height determinations, as well as geometry optimizations and reaction thermodynamics, essentially covering all kinds of routine calculations for thermochemistry. This is the first time these two training methodologies have been directly compared within the same framework, providing valuable insights into their relative performance and applicability. The outcomes have robustly validated our strategy and underscored the practical utility of our models. Significantly, our results have demonstrated that the integration of XPaiNN with the SQM method GFN2-xTB²⁰ yields a highly promising general-purpose atomistic ML model, namely XPaiNN@xTB, that boosts not only high accuracy but also transferable performance across diverse chemical contexts.

Construction of XPaiNN models

Related works

By treating atomic systems as graph-structured data, GNNs have demonstrated remarkable performance in end-to-end atomistic ML applications.²¹ The inclusion of rotation and inversion equivariance has led to the advent of equivariant GNNs,^{15,17,22-25} which have made significant strides in virtually every aspect when compared to their invariant equivalents.^{26,27} Notably, equivariant GNN models have been reported to exhibit superior data efficiency in achieving

comparable (or even better) levels of accuracy.²³ An overview of group equivariance and equivariant GNNs is provided in the **SI**.

One primary critique of equivariant GNNs lies in the computationally intensive tensor product operations for generating equivariant hidden features, which notably impairs model efficiency.²⁵ Acknowledging this limitation, Schütt and co-workers introduced the PaiNN model,¹⁷ which circumvents this problem of tensor contraction convolutions. PaiNN preserves equivariance in the neural network by implementing separate transformation rules for scalar and Cartesian vector feature channels. TensorNet,²⁸ another equivariant GNN, adheres to a similar design principle, focusing on the generation and transformation of different components of rank-2 tensors in Cartesian representation, thereby achieving improved performance over PaiNN.

The approach of Δ -ML,²⁹⁻³² has long been pivotal in enhancing the transferability of atomistic ML models, where a cheaper method, often DFT, is employed as the baseline method for calibrating the target property with higher accuracy that would otherwise be attainable only with Coupled-Cluster Singles Doubles with perturbative Triples (CCSD(T)), or with high-quality experiment results. The renaissance of SQM methods represents a recent direction,^{33,34} which enables computational speeds several orders of magnitude faster compared to conventional DFT calculations, albeit with a trade-off involving reduced accuracy. As systematic approximations are incorporated, these SQMs are drawing new attention as the baseline method in Δ -ML models.^{35,36}

There are two prominent series of atomistic ML methods, aiming for transferable and accurate modeling of general-purpose. One belongs to the ANI potential family,⁹⁻¹² developed using the classical framework of Behler-Parrinello neural network.³⁷ The other key player is the OrbNet family,¹³⁻¹⁵ introduced by Miller’s group, which embodies a category of QM-informed ML models, using features, such as the single-particle Hamiltonian,³⁸ generated from QM calculations as inputs for GNNs.³⁸⁻⁴⁰ Of note, AIQM1¹² and OrbNet-Equi¹⁵ represent the SOTA with remarkable accuracy in chemical benchmark tests. Both of these models adopt

the Δ -ML strategy, wherein SQM methods serve as the baseline methods.

XPaiNN architecture

The architecture of XPaiNN is illustrated in Figure 1. As shown, XPaiNN inherits its basic structure from PaiNN, consisting of three primary components: **Embedding**, **Message Passing Convolution** (involving both **Message Passing** and **Node Updating**), and the **Output** block. In order to bolster the model capacity, one major change to the original PaiNN framework is to substitute the vector feature channel \mathbf{v} in PaiNN with a spherical feature channel $\boldsymbol{\chi}$ in XPaiNN, an innovation explained further in subsequent sections. Moreover, we have devised a novel set of element-wise scalar embeddings for initializing node features within graph data, intended to reflect the periodic table trend for properties of chemical elements. Detailed descriptions regarding the remaining of the model architecture are provided in the SI.

Embedding. We employ a set of precomputed element-specific features \mathbf{e}^{Z_A} for each atomic species A, identified by its atomic number Z_A , which differs from the conventional one-hot embedding typically used in atomistic ML models. These embedding features are linearly transformed to the hidden node features \mathbf{x}_i^0 , serving as the initial input to the scalar feature channel of XPaiNN for the i -th node. Additionally, the input to the spherical feature channel, $\boldsymbol{\chi}_i^0$ is initialized with all zeros.

$$\mathbf{x}_i^0 = \mathbf{e}^{Z_i} \mathbf{W}^\top + \mathbf{b} \quad (1)$$

$$\boldsymbol{\chi}_i^0 = \bigoplus_l \boldsymbol{\omega}_i^{(l)} = \mathbf{0} \quad (2)$$

Message Passing. The improvement of TensorNet, as compared to PaiNN, illustrates the significance of higher l -order feature channels in enhancing the model capacity of an equivariant GNN method. Meanwhile it is much easier to handle l -order channels in spherical representation than in Cartesian form. Consequently, we extend the original vector feature

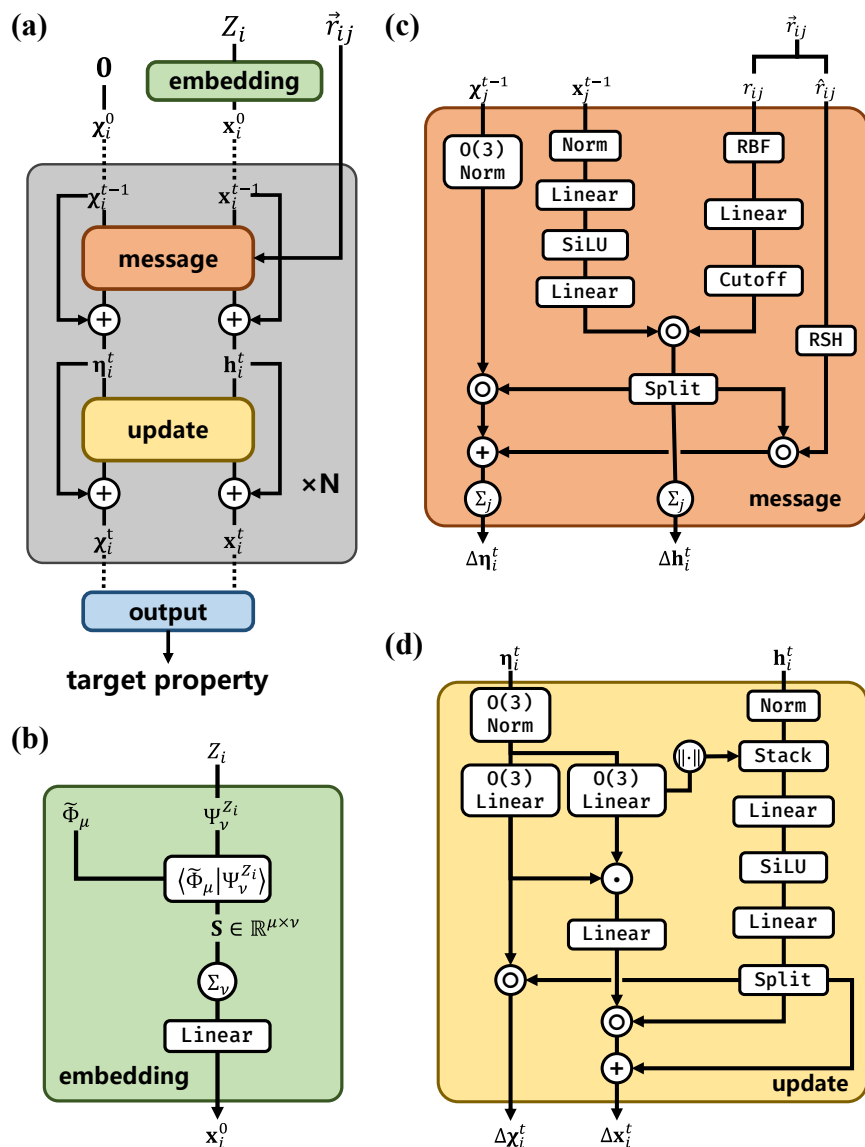


Figure 1: **Schematic diagram of XPaiNN model architecture.** (a) Architecture overview. (b) Atom embedding layer. (c) Message passing layer. (d) Node update layer.

channel \mathbf{v}_i ($l = 1$) of PaiNN to a spherical feature channel $\boldsymbol{\chi}_i$ of XPaiNN. As shown in Eq.(2), $\boldsymbol{\chi}_i$ is constituted by the direct sum of irreducible representations (Irreps) $\boldsymbol{\omega}_i^{(l)}$ corresponding to angular momentum number l , which is a hyperparameter of great significance in XPaiNN, offering flexibility in dimension adjustment. This strategy amplifies model capacity desirably, while only moderately increases the number of trainable parameters, thereby preserving the computational efficiency inherent to PaiNN. To incorporate this change in the feature channels, we use an equivariant filter by expanding the inter-atomic directions $\hat{\mathbf{r}}_{ij}$ with real spherical harmonics (RSH) in the **Message Passing** layer. This filter is responsible for directly generating equivariant features of the required order and shape. The subsequent message passing routine mirrors that of PaiNN, where both scalar and spherical features are updated through aggregation over transformed features of neighboring atoms $\mathcal{N}(i)$, which can be expressed as

$$\mathbf{h}_i^t = \mathbf{x}_i^{t-1} + \sum_{j \in \mathcal{N}(i)} f_m^t(\mathbf{x}_j^{t-1}, \mathbf{r}_{ij}) \quad (3)$$

$$\boldsymbol{\eta}_i^t = \boldsymbol{\chi}_i^{t-1} + \sum_{j \in \mathcal{N}(i)} \phi_m^t(\mathbf{x}_j^{t-1}, \boldsymbol{\chi}_j^{t-1}, \mathbf{r}_{ij}) \quad (4)$$

where the concrete operations of message functions f_m and ϕ_m are illustrated in Figure 1(c).

Datasets and training

The QM9 dataset is widely used for assessing the performance of atomistic ML models in predicting molecular properties. It contains 133,885 small organic molecules at the respective DFT-optimized geometry, with target properties computed at the same level.¹⁸ To benchmark the model capacity of the XPaiNN framework, we also employ the QM9 dataset,¹⁸ capitalizing on existing comparisons among various atomistic ML models.

Adequate training data is a prerequisite for the development of a general-purpose potential energy surface model. Notably, most of the ANI potentials are developed based on the ANI-1x dataset,⁴¹ encompassing 5 million single organic molecules composed of C, H, N, and O. Conversely, the OrbNet Denali dataset¹⁴ contains 2.3 million molecular conformations

covering 17 elements, with a subset serving as the training set for OrbNet-Equi. Furthermore, we believe that central to constructing an accurate atomistic ML model of practical value are considerations regarding the breadth of chemical space coverage and the reliability of DFT-calculated labels.

With these considerations in mind, this work utilizes the SPICE dataset¹⁹ as its foundation. Comprising up to 1.1 million configurations of small organic molecules, dimers, dipeptides, and solvated amino acids, this dataset covers a wide range of covalent interactions, as well as NCIs in main-group chemistry. It furnishes total energies, forces, and additional properties computed at the ω B97M-D3(BJ)^{42,43}/def2-TZVPPD level of theory, which, to the best of our knowledge, is the first QM dataset of this size with such an accuracy. SPICE further ensures comprehensive coverage of relevant conformational landscapes for each sampled molecule, with guidelines conducive to further data augmentation.¹⁹ Thus, this dataset is anticipated to be an ideal choice for training accurate potential energy model for general-purpose in a data-efficient way. The training set used in this work is a curated subset of SPICE, including only neutral, closed-shell molecular systems featuring H, C, N, O, F, P, S, Cl, Br, and I (see the **SI** for more details).

On top of this selected SPICE dataset, we trained two models: one that directly fits target labels of energies and forces, and the other that adopts the Δ -ML strategy, using the SQM method GFN2-xTB²⁰ as the baseline method. Consequently, the energy and force evaluations by the latter model, XPaiNN@xTB, can be decomposed into two parts:

$$E_{total}^{XPaiNN@xTB} = E^{XPaiNN} + E^{GFN2-xTB} \quad (5)$$

$$\vec{F}_A^{XPaiNN@xTB} = \vec{F}_A^{XPaiNN} + \vec{F}_A^{GFN2-xTB} \quad (6)$$

Training for this model focuses on the residuals between outputs of the baseline method and those of the target level of theory, with other hyper-parameters and training strategies remaining consistent as the direct-learning model. This setup enables a clear illustration

of the advantages and drawbacks between direct-learning and the Δ -ML strategy through comparative testing performance. Detailed training methodologies for these models are outlined in the **SI**, along with hyper-parameters provided in Tables S1-S3.

Results

Performance on QM9

The results of test performance for XPaiNN across the 12 prediction tasks within the QM9 dataset are summarized in Table 1, along with those reported by other GNN and equivariant GNN models. As evident, XPaiNN demonstrates low test errors across all tasks, positioning it amongst the top performers against the QM9 benchmarking. Notably, substantial and consistent advancements are discernible when contrasting the results of XPaiNN with those of PaiNN. Specifically, in properties pertaining to frontier orbitals, namely, ϵ_{HOMO} , ϵ_{LUMO} and $\Delta\epsilon$, the mean absolute errors (MAEs) in these subsets are reduced by an average of 18%. With respect to thermodynamic properties, including U_0 , U , H and G , an additional improvement averaging 0.4 meV is accomplished, a significant refinement given the already insignificant error margins. Further ablation studies, as detailed in Table S4 in the **SI**, suggest that these improvements predominantly derive from the incorporation of higher-order features in the spherical channels of XPaiNN, demonstrating the success of our model architecture.

Results summarized in Table S5 of the **SI** uncover a further dramatic improvement over XPaiNN on thermodynamic properties with XPaiNN@xTB, demonstrating the enhanced model capacity and data efficiency of the Δ -ML strategy.

Performance on downstream tasks

To explore model transferability, we apply the two potential energy models, XPaiNN and XPaiNN@xTB, to a variety of downstream tasks, involving the calculations of relative energetic properties such as reaction energies, barrier heights, and NCIs, as well as geometry

Table 1: Mean absolute errors on QM9 test set.^a

Task	Unit	SchNet ^b	DimeNet++ ^b	PaiNN ^b	SphereNet ^b	Equiformer ^b	XPaiNN ^c
μ	D	0.033	0.030	0.012	0.024	0.011	0.011±0.000
α	a_0^3	0.235	0.044	0.045	0.045	0.023	0.042±0.000
ϵ_{HOMO}	meV	41	24.6	27.6	22.8	15	21.7±0.2
ϵ_{LUMO}	meV	34	19.5	20.4	18.9	14	16.4±0.2
$\Delta\epsilon$	meV	63	32.6	45.7	31.1	30	38.1±0.7
$\langle R^2 \rangle$	a_0^2	0.073	0.331	0.066	0.268	0.251	0.065±0.002
zpve	meV	1.7	1.21	1.28	1.12	1.26	1.20±0.01
U_0	meV	14	6.32	5.85	6.26	6.59	5.43±0.08
U	meV	19	6.28	5.83	6.36	6.74	5.53±0.03
H	meV	14	6.53	5.98	6.33	6.63	5.41±0.03
G	meV	14	7.56	7.35	7.78	7.63	6.85±0.06
C_v	cal/mol/K	0.033	0.023	0.024	0.0215	0.023	0.023±0.000

^a Best results in **bold**;

^b Results are taken from Ref. 25;

^c Averaged over four models.

optimizations and reaction thermodynamics calculations.

For comparison, we consider three SOTA atomistic ML models, ANI-1ccx,¹⁰ AIQM1,¹² and OrbNet-Equi,¹⁵ where their performances on these benchmarks are documented. Furthermore, the results from some recent SQM methods, i.e., GFN-xTB,⁴⁴ GFN2-xTB,²⁰ and ODM2,⁴⁵ are also included, as they served as the baseline methods for OrbNet-Equi, XPaiNN@xTB, and AIQM1, respectively. Additionally, we present results from the DFT method ω B97M-D3(BJ),^{42,43} which represents the target level of theory for our models. It is important to acknowledge that the accuracy and transferability of these ML models vary as a result of differences in model architecture and training regimens, reflecting model capacity and data efficiency. Specifically, the ANI models, ANI-1ccx and AIQM1, have been trained on energies and forces at the ω B97X⁴⁶ level and are subsequently fine-tuned via transfer learning to approximate the CCSD(T)/CBS level for energy predictions, albeit being limited to compounds comprising H, C, N, and O.^{10,12} Meanwhile, OrbNet-Equi has been trained on energy labels at the ω B97X-D3/def2-TZVP level, covering a broader range of chemical elements.¹⁵

Furthermore, we apply the two models, XPaiNN and XPaiNN@xTB, to reaction enthalpy

calculations, wherein second-order derivatives of energy with respect to atomic positions are necessitated by the computations of vibrational frequencies and then thermo-corrections. This validates the potential of our models as a viable alternative for routine QM calculations of reaction thermodynamics, aiming to offer both high efficiency and accuracy.

GMTKN55 benchmark. To assess the models’ performance in predicting relative energies, we examine XPaiNN and XPaiNN@xTB utilizing GMTKN55,⁴⁷ which is a benchmark widely acknowledged for its effectiveness in evaluating electronic structure methods. This dataset contains 55 subsets designed to evaluate various aspects of comprehensive main-group chemistry, targeting General Main-group Thermochemistry, Kinetics, and Non-covalent interactions.⁴⁷ It employs reference values often calculated at the gold-standard CCSD(T)/CBS level of theory. Our focus lies on subsets composed exclusively of neutral, closed-shell molecules, comprising elements of H, C, N, O, F, P, S, Cl, Br, and I, in accordance with the design of XPaiNN. Consequently, from the subsets within GMTKN55, 21 have been selectively considered, and the overall error analyses are summarized in Table 2. In order to quantify subset-specific errors, we employ the Weighted Total Mean Absolute Deviation of the second type (WTMAD-2), as defined in Ref. 15. The detailed formula is outlined in the **Computational Details** section in **Material and Methods**. Illustrations of the chosen subsets are provided in Table S6 in the **SI**, with further specifics available elsewhere.⁴⁷

As shown in Table 2, while the overall WTMAD-2 values are tightly contested (17.20 vs. 18.45 kcal/mol), XPaiNN outperforms GFN2-xTB in the majority of subsets. Major advantages are evident in scenarios involving energy differentials between molecules at nearly equilibrium geometries, notably in subsets such as FH51, TAUT15, DARC, ISO34, and those focusing on intramolecular NCIs. These achievements can largely be attributed to the model capacity of the XPaiNN architecture as well as the high-quality training dataset, as evidenced by the performance of the target ω B97M-D3(BJ) method. Encouragingly, XPaiNN also exhibits competitiveness akin to the AIQM1 model, as validated by outcomes within the HCNO subset, the domain of proficiency of the AIQM1 model. While AIQM1 shows

Table 2: WTMAD-2 for various methods on the selected subsets of GMTKN55.^a Unit in kcal/mol.

	ω B97M-D3(BJ)	GFN-xTB	GFN2-xTB	AIQM1	OrbNet-Equi	XPaiNN	XPaiNN@xTB
Basic properties and reaction energies for small systems							
FH51	1.86	22.09	20.92	-	9.40	8.25	6.80
TAUT15	5.41	108.14	18.31	-	21.78	7.81	8.18
Reaction energies for large systems and isomerization reactions							
DARC	1.88	27.70	31.10	1.11	1.32	2.73	1.85
BSR36	6.55	8.22	9.69	3.71	24.07	4.13	5.94
CDIE20	8.91	28.63	25.26	-	16.00	18.85	11.74
ISO34	2.38	24.56	26.93	1.70	7.28	3.30	2.07
C60ISO	7.90	4.56	3.36	27.71	2.32	23.98	5.09
Reaction barrier heights							
BHROT27	2.12	21.55	10.59	-	5.40	6.72	3.57
PX13	2.69	14.14	4.66	-	22.08	50.72	20.26
WCPT18	1.81	8.61	6.24	-	12.10	10.08	3.97
Intermolecular noncovalent interactions							
ADIM6	6.82	17.06	19.48	14.97	4.64	4.93	8.55
S22	1.97	10.36	5.90	6.76	4.05	4.71	2.07
S66	2.15	11.16	7.60	6.45	5.16	4.12	2.91
HAL59	5.51	16.64	15.79	-	33.50	90.46	57.08
Intramolecular noncovalent interactions							
IDISP	5.70	26.08	27.09	13.24	19.66	9.50	7.12
ACONF	3.92	20.52	5.97	8.07	1.64	5.55	2.66
Amino20x4	6.12	25.97	22.23	-	7.01	13.85	6.99
PCONF21	11.76	76.04	61.62	27.38	18.00	33.25	20.25
MCONF	2.46	16.51	19.70	4.13	5.39	9.90	4.31
SCONF	1.81	30.93	20.30	11.68	6.59	13.86	9.18
BUT14DIOL	4.11	19.36	25.36	9.17	12.02	3.78	2.56
WTMAD-2 (HCNO) ^b	3.81	19.60	19.71	7.84	9.35	7.46	4.64
WTMAD-2 (Total) ^c	4.15	22.41	18.45	-	11.77	17.20	10.44

^a Best in **bold** excluding DFT.

^b Overall WTMAD-2 for subsets consists of H, C, N and O, the AIQM1 collection.

^c Overall WTMAD-2 for the listed subsets as a whole, see **Computational Details**.

remarkable accuracy in predicting reaction energies as in DARC, BSR36, and ISO34, but falls short in accurately depicting NCIs as in ADIM6, IDISP, PCONF21, and SCONF. In contrast, XPaiNN attains an overall accuracy on par with AIQM1 within this HCNO subset, being better in modeling intermolecular NCIs of ADIM6, S22 and S66. As the training process embodies these NCIs within conformation energies, thereby enhancing the model’s descriptive power in this area.

Meanwhile, it becomes apparent that XPaiNN faces challenges with systems that exhibit chemical characteristics that are different from its training data. This includes large, highly conjugated systems such as fullerene (C60ISO), molecular configurations at transition states, specifically the determination of reaction barrier heights in proton transfers (PX13 and WCPT18), intermolecular NCIs mediated by halogen bonds (HAL59), and intramolecular NCIs within polypeptide chains (PCONF21). Some of these challenges are similarly encountered by AIQM1, highlighting shared limitations in handling chemically or structurally different systems as compared to their training data.

Notably, XPaiNN@xTB and OrbNet-Equi perform fairly well on these assessments with an overall improved WTMAD-2 of 10.44 and 11.77 kcal/mol, respectively. In several subsets, they approach the level of accuracy of the targeted DFT method. Of great significance, it is seen that for the intricate systems that pose challenges to direct-learning models, these Δ -ML models exhibit an enhanced transferability. Notably, XPaiNN@xTB improves upon XPaiNN, achieving results that rival DFT-level accuracy as in C60ISO and WCPT18, although some advancements remain partial as in PX13 and HAL59. These findings underscore the significance of incorporating physical principles into atomistic ML models to ensure robust and transferable predictive power. While SQM methods stand out as efficient and appealing choices of the baseline methods, their accuracy in turn impacts the models’ performance, as evidenced in subsets such as TAUT15 and PCONF21. All in all, the commendable accuracy of the Δ -ML models on the GMTKN55 benchmark is a synergistic outcome of both model training strategies and the choice of SQM baselines.

The barrier height benchmark for pericyclic organic reactions. Reaction barrier height, a key factor in determining reaction kinetics, is defined as the energy difference between the reactant and the transition state (TS). A prior study⁴⁸ revealed limitations in the model capacity of AIQM1 to accurately predict barrier heights for pericyclic organic reactions. Consequently, we assess our models using the same dataset, which is a subset of the BH9 dataset,⁴⁹ where reference values have been calculated utilizing the DLPNO-CCSD(T)/CBS level of theory. Our evaluation involves not only the barrier heights for both the forward and reverse reactions but also 102 reaction energies in total. The results are presented in Table 3.

Table 3: Mean absolute errors on predicting reaction barrier heights and energies on the selected reactions of BH9.^a Unit in kcal/mol.

	ω B97M-D3(BJ)	XPaiNN	XPaiNN@xTB	ANI-1ccx	AIQM1	GFN2-xTB	ODM2
Forward Barrier	1.13	24.38	4.93	8.06	13.24	12.39	7.51
Backward Barrier	0.96	23.12	4.93	7.24	13.70	4.67	8.74
Reaction Energy	1.13	2.71	1.36	3.56	2.05	14.68	4.77

^a Containing closed-shell compounds of H, C, N and O, mainly consists of Diels-Alder and other Pericyclic reactions.

Clearly, the accuracy of the ML models in predicting barrier heights of pericyclic reactions is not consistently reliable. Among these, XPaiNN performs the least satisfactorily. The performance of ANI-1ccx is comparable to that of SQM methods, while AIQM1 fails to outperform its baseline, ODM2. However, XPaiNN@xTB demonstrates a fairly good accuracy, with MAD of 4.93 kcal/mol for both forward and reverse barriers, marking a substantial improvement over the standalone XPaiNN, whose deviations exceed 20 kcal/mol. Reflecting on the performance of AIQM1, we attribute the enhanced transferability of XPaiNN@xTB to the synergistic effects of the Δ -ML strategy and the power of equivariant GNNs. This serves as further conclusive evidence supporting our benchmark results of GMTKN55.

Noteworthy, Table 3 reveals a clear discrepancy in the performance of all ML models when comparing their predictions of reaction energies versus barrier heights. While these models are outstanding at estimating reaction energies from equilibrium structures, their

performances degrade in predicting reaction barriers, which can undoubtedly be attributed to the absence of TS structures within the training dataset SPICE. This deficiency emphasizes the necessity to incorporate TS structures into the training set when developing general-purpose atomistic ML models for consistent description of a chemical reaction along the reaction pathway.

The S66x8 and Torsion benchmarks. We use the S66x8⁵⁰ and Torsion⁵¹ datasets as benchmarks to further evaluate the performances of XPaiNN and XPaiNN@xTB. Both datasets contain over 60 organic molecular systems, each with a diverse range of conformational profiles. Specifically, the S66x8 dataset focuses on intermolecular NCIs, containing hydrogen bonding, π - π stacking, X - π interactions, and aliphatic dispersion interactions, etc., while the Torsion dataset emphasizes intramolecular rotational conformations. Both datasets employ highly accurate CCSD(T)/CBS calculations as energy references. In order to facilitate a comparison with the ANI potentials, we concentrate on systems composed of H, C, N, and O, which results in a selection of 45 profiles from the original 62 in the Torsion dataset.

The overall error performances are depicted in Figure 2, while detailed statistical analyses are provided as the zip file in the **SI**. As can be seen from Figure 2 **(a)** to **(d)**, our models distinguish themselves in these predictions, exhibiting small MAEs and tight error distributions, surpassing the performance of the SQM methods. As is clear, our ML models perform fairly well on the Torsion dataset, given their extensive training on conformational variations using the SPICE dataset.¹⁹ While ANI-1ccx is less accurate in dealing with intermolecular NCIs, the AIQM1 model shows a better performance in this regard. This disparity in handling intermolecular NCIs is further highlighted when comparing XPaiNN with XPaiNN@xTB. More intriguingly, as shown in Figure 2**(f)**, XPaiNN@xTB accurately predicts the torsional conformations of N-(furan-2-yl)acetamide, even in the presence of unphysical barriers as predicted by GFN2-xTB, indicating the robustness of XPaiNN@xTB in delineating intricate potential energy surfaces of NCIs.

The ROT34 benchmark. Geometry optimization of molecules is a common practice

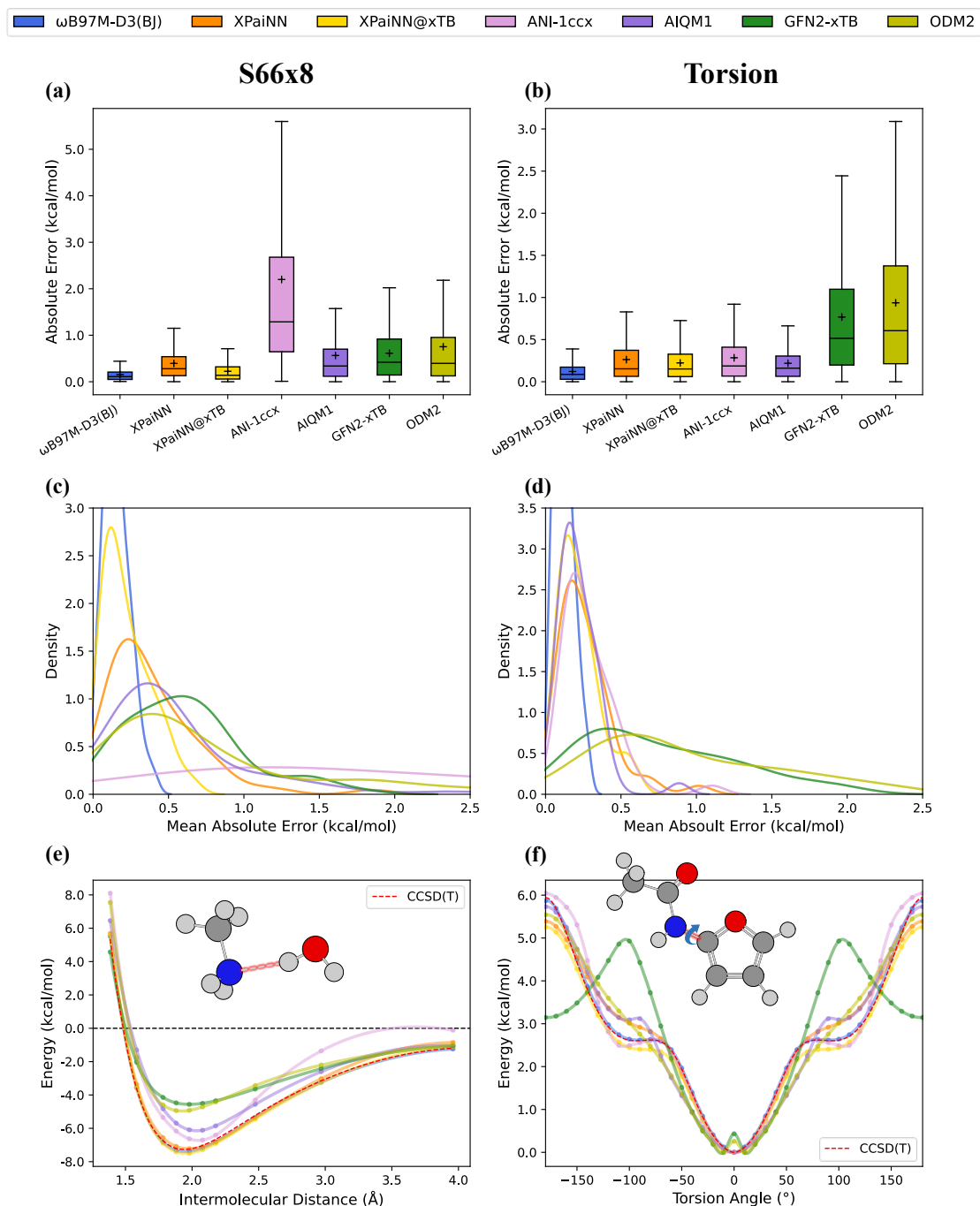


Figure 2: **Results of different methods on S66x8 and Torsion.** (a) (b) Box plots for absolute error of different methods. The horizontal line is the median and the “+” symbol is the mean. (c) (d) MAE distribution of different methods. The MAEs are Averaged by molecules or molecule pairs. (e) Example of intermolecular interaction between methylamine and water. The potential energy curves are shown as functions of the N-H hydrogen bond length. (Two additional coordinates are included, see **Computational Details**.) (f) Example of torsion conformation for N-(furan-2-yl)acetamide. The conformational curves are shown as functions of the N-C torsion angle.

in computational chemistry, involving an iterative procedure to find the structure that minimizing the energy. This necessitates the calculation of energy gradients with respect to the geometry, a task that can be computationally intensive when employing a first-principles method. ML models offer a means to expedite this process. Here, we validate our models, XPaiNN and XPaiNN@xTB, to undertake geometry optimization tasks on a selection of 12 organic molecules from the ROT34 dataset.⁵² The reference geometries for these molecules have been established using the SCS-MP2⁵³/def2-QZVP level of theory, which is known to closely align with experimental rotational constant data,⁵² ensuring a high degree of accuracy for benchmarking purposes.

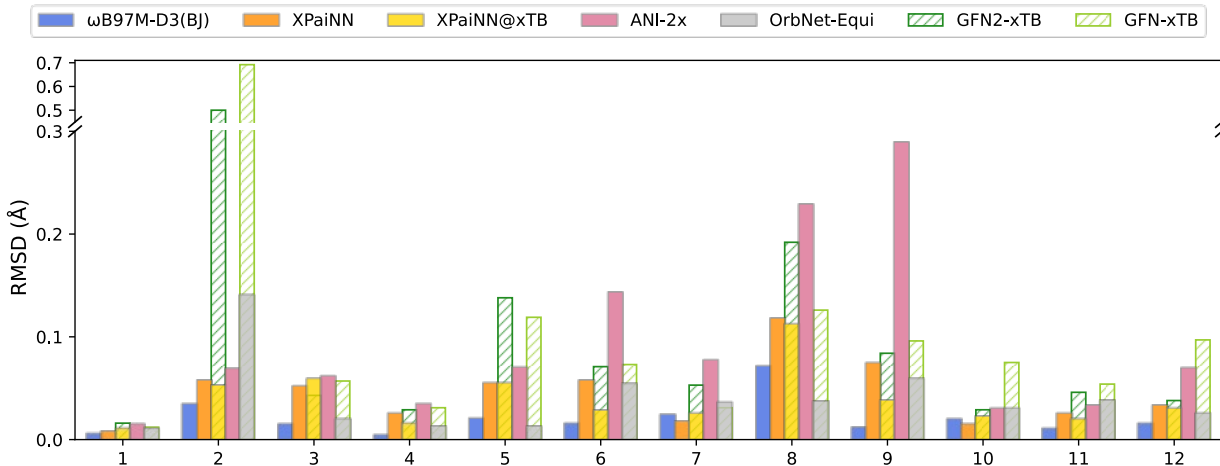


Figure 3: Root-mean-square deviations of different methods’ optimized structures against reference structures for the 12 molecules in ROT34 dataset. Compound 9 is in the training dataset.

The root-mean-square deviations (RMSDs) of each optimized geometry, as determined by various methods with respect to the reference geometry, are depicted in Figure 3. Both XPaiNN models yield superior geometric structures as compared to the SQM methods and the ANI-2x model. Specifically, they achieve average RMSDs of 0.045 Å and 0.039 Å, respectively, which are on par with that of OrbNet-Equi (0.040 Å) and close to the target DFT accuracy (0.021 Å). This notable performance is attributed to the comprehensive coverage of molecular conformations included in the training dataset. Consequently, our models exhibit a promising capability to perform geometry optimizations with a fairly good accuracy but at

a substantially low cost.

The reaction thermodynamics test. We proceed to challenge our models with the estimation of reaction enthalpies, a task that is more demanding. This endeavor necessitates the calculation of vibrational frequencies at the respectively optimized molecular structure, which involves computing second-order derivatives of energy with respect to atomic positions, a process that is computationally expensive when employing sophisticated methods. Consequently, more cost-effective alternatives are frequently sought for approximating thermochemical effects.⁵⁴ We show here that our ML models present a viable solution by facilitating these routine calculations concurrently, offering a significantly reduced computational cost while still maintaining a satisfactory level of accuracy.

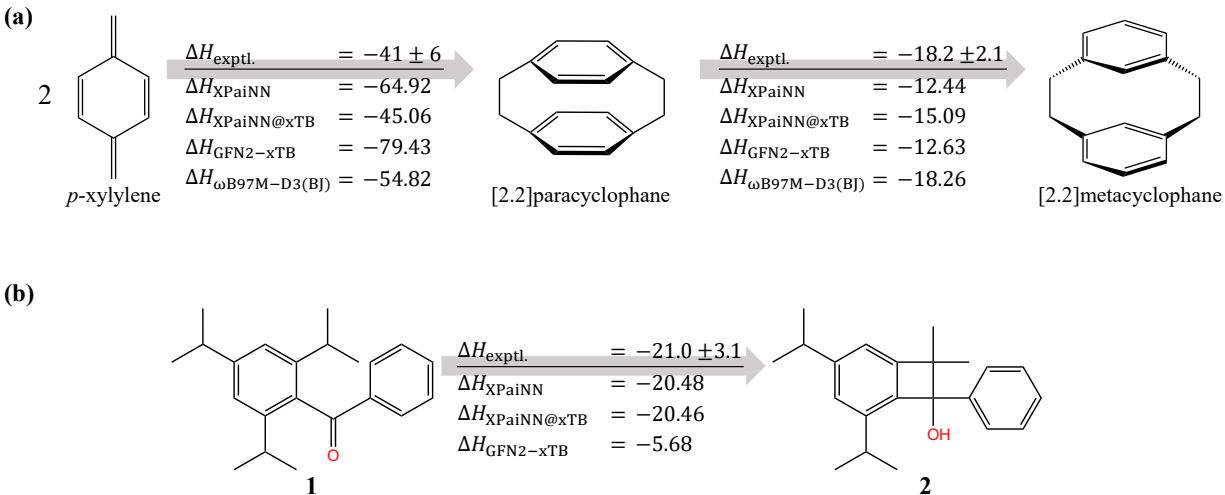


Figure 4: Reaction enthalpies given by different methods along with the corresponding experimental values. Unit in kcal/mol. **(a)** Formation of [2.2]paracyclophane from *p*-xylylene and subsequent isomerization to [2.2]metacyclophane. **(b)** Isomerization between **1** (2,4,6-triisopropylbenzophenone) and **2** (3',5'-diisopropyl-4,4-dimethyl-3-phenyl-1,2-benzocyclobuten-3-ol).

Figure 4(a) depicts an example for the dimerization of *p*-xylylene to [2.2]paracyclophane, followed by its isomerization to [2.2]metacyclophane. Here, we employ both XPaiNN and XPaiNN@xTB for geometry optimizations and subsequent vibrational frequency calculations of the involved molecules to ascertain the reaction enthalpies. For comparison, similar computations were also carried out using GFN2-xTB and the ω B97M-D3(BJ) method. The

results, along with experimental reference values,⁵⁵⁻⁵⁷ are presented in Figure 4(a). Our models demonstrate enhanced accuracy in estimating reaction enthalpies compared to GFN2-xTB. Notably, the predictions from XPaiNN@xTB closely agree with the experimental values and rival those obtained from the DFT calculations. It is crucial to highlight that employing a high-level DFT approach such as ω B97M-D3(BJ)/def2-TZVPPD requires 3.7 CPU-days on a machine with Intel Xeon Platinum 9282 CPU, whereas our ML models accomplish the same tasks in mere 140 CPU-seconds using one Intel Xeon Gold 6254 CPU and one NVIDIA RTX2080 GPU, thereby achieving a striking reduction in computational cost.

Figure 4(b) gives another illustrative case, involving enthalpy calculations for the isomerization between compounds **1** and **2**, a process too computationally demanding to be practically undertaken using high-level DFT coupled with a large basis set. Conversely, such calculations pose no challenge to our models, and they yield results that are consistent with experimental values.⁵⁸ Remarkably, even though our models are trained without explicitly fitting the Hessian matrix, they manage to attain a satisfactory level of accuracy in predicting thermodynamic properties. These results serve as compelling demonstrations of the practical utility of the XPaiNN@xTB model, offering DFT-level accuracy in routine QM calculations with the computational efficiency akin to SQM methods.

Discussion

In this work, we propose XPaiNN, an equivariant GNN, designed for constructing a versatile atomistic ML model of general-purpose. The major extension from the original PaiNN to XPaiNN lies in replacing vector feature channel \mathbf{v} of the former with spherical feature channel χ in the latter, with dual objective of enhancing model capacity and data efficiency while preserving computational efficiency. The outcomes from evaluations on well-established benchmark dataset QM9 decisively endorse our design principles underlying this neural network model.

To address the challenge of model transferability, we have trained two XPaiNN models, applying both direct-learning and Δ -ML strategy on the SPICE dataset. This is the first time these two training methodologies have been directly compared within the same framework, offering valuable insights into their relative performance and applicability. The direct-ML model exhibits commendable performance chemically similar systems at near-equilibrium structures, showing a competitive performance of the AIQM1 model. Meanwhile, the Δ -ML model demonstrates enhanced accuracy and transferability across extensive tests, particularly for systems with diverse chemistry, including large conjugated compounds, intermolecular NCIs, and transition states. This enhancement is achieved by incorporating the SQM method GFN2-xTB as the baseline. The resultant model, XPaiNN@xTB, has been shown to offer an accurate alternative to high-level DFT methods in routine QM calculations at the speed and cost of SQM methods.

We attribute the current success to the incorporation of physical (fundamental symmetries encoded in equivariant GNNs) and chemical (systematically approximated SQM method as the baseline) priors as inductive biases during model construction. We conclude that the quality of training data and the model’s architecture are equally crucial in achieving desired levels of accuracy and efficiency.

Although the current XPaiNN has not explicitly considered electronic degrees of freedom, such as charge and spin, we are actively exploring ways to integrate these effects so as to broaden the model’s applicability across a wider range of chemical spaces.^{40,59,60} Furthermore, GNN models are inherently adaptable for extended training through active learning strategies,⁶¹ a beneficial trait for developing general-purpose atomistic ML models. Overall, we envision this work contributing significantly to the ongoing development of such models, offering tangible benefits to various scientific disciplines.

Materials and Methods

Model training, testing and inference with XPaiNN framework were performed using the XequiNet package (see **Code Availability**), built upon PyTorch 2.0.1,⁶² torch-geometric 2.3.1⁶³ and e3nn 0.5.1.⁶⁴ The contributions of the baseline GFN2-xTB in XPaiNN@xTB were calculated with TBlite 0.3.0.⁶⁵ Geometry optimizations and vibrational frequency calculations for these models were carried out using geomeTRIC 1.0⁶⁶ and PySCF 2.4.0,⁶⁷ respectively.

Computational Details

For benchmark on GMTKN55, the subset-wise error metric is define as¹⁵

$$\text{WTMAD-2}_i = \frac{1}{N_i} \sum_j \text{WTAD}_{i,j} \quad (7)$$

$$\text{WTAD}_{i,j} = \frac{56.84 \text{ kcal/mol}}{\frac{1}{N_i} \sum_j |\Delta E_{i,j}|} \cdot \left| \Delta E_{i,j} - \Delta \hat{E}_{i,j} \right| \quad (8)$$

where $\text{WTAD}_{i,j}$ refers to the weighted mean absolute deviation of j -th reaction within subset i , N_i is the total number of reactions in subset i , while $\Delta E_{i,j}$ and $\Delta \hat{E}_{i,j}$ correspond to the reference and predicted reaction energies, respectively. 56.84 kcal/mol is the averaged absolute reaction energy across the entirety of the GMTKN55 dataset. It should be noted that the original definition for $\text{WTAD}_{i,j}$, i.e., Equation (38) in Ref. 15 is incorrect; Eq.(8) herein reflects the actual formula for its computation. Furthermore, the overall WTMAD-2 for both the whole dataset and the curated selection was evaluated according to

$$\text{WTMAD-2} = \frac{1}{\sum_i N_i} \sum_{i,j} \text{WTAD}_{i,j} \quad (9)$$

The subset-wise WTMAD-2 values in Table 2 for the SQM methods and other ML models were retrieved from Ref. 15. The corresponding values for ω B97M-D3(BJ) were calculated using ORCA 5.0.4,⁶⁸ while those for the AIQM1 model were attained with MLatom, version

2.0.⁶⁹

For the results pertaining to the S66x8 and Torsion benchmark datasets, calculations for GFN2-xTB were performed with xTB 6.4.0.⁷⁰ Those for AIQM1, ANI-1ccx, and ODM2 were gathered from Ref. 12. For the ω B97M-D3(BJ)/def2-TZVPPD calculations, ORCA 5.0.4 was utilized. For Torsion benchmark, each molecule underwent constrained optimization within its profile, with fixed dihedral angles, to determine the conformational energy. In Figure 2(e), two conformations at distances of 1.38 Å and 1.58 Å were added to the original profile, where the geometries and reference values associated with these conformations were taken from the S66x10 dataset.⁷¹ The values for AIQM1 and ANI-1ccx as displayed in the figure were calculated using MLatom 2.0, while those for ODM2 were calculated using MNDO.⁷²

For the prediction of barrier heights in the BH9 dataset, the results for GFN2-xTB were computed using xTB 6.4.0. All other results in this context were sourced from Ref. 49. Regarding geometry optimizations, the optimized structures for SQM methods, ANI-2x, and OrbNet-Equi were obtained from Ref. 48. Calculations for ω B97M-D3(BJ) were performed using ORCA 5.0.4. In the case of reaction enthalpies, all reaction enthalpy values were determined using the aforementioned software programs and packages.

Code Availability

The XPaiNN model is available in XequiNet package from Github: <https://github.com/X1X1010/XequiNet>.

Data Availability

Partitioned QM9 dataset in HDF5 format, trained models on QM9, and optimized structures of ROT34 have been deposited in Zenodo (<https://zenodo.org/records/12745133>). Detailed and additional results on downstream benchmarks of GMTKN55, S66x8, Torsion and BH9 are provided with this work as supporting information. Requests for trained models on SPICE should be addressed to Jianming Wu and Xin Xu.

Acknowledgement

This project is supported by the National Natural Science Foundation of China (Grant 22393911, 22233002 and 21373053), and Innovation Program for Quantum Science and Technology (2021ZD0303305). The authors appreciate both the High-End Computing Center and the CFFF platform of Fudan University for generously providing computational resources.

References

- (1) Hohenberg, P.; Kohn, W. Inhomogeneous electron gas. *Phys. Rev.* **1964**, *136*, B864–B871.
- (2) Kohn, W.; Sham, L. J. Self-consistent equations including exchange and correlation effects. *Phys. Rev.* **1965**, *140*, A1133–A1138.
- (3) Marzari, N.; Ferretti, A.; Wolverton, C. Electronic-structure methods for materials design. *Nat. Mater.* **2021**, *20*, 736–749.
- (4) Butler, K. T.; Davies, D. W.; Cartwright, H.; Isayev, O.; Walsh, A. Machine learning for molecular and materials science. *Nature* **2018**, *559*, 547–555.
- (5) Margraf, J. T. Science-Driven Atomistic Machine Learning. *Angew. Chem. Int. Ed.* **2023**, *62*, e202219170.
- (6) Unke, O. T.; Chmiela, S.; Sauceda, H. E.; Gastegger, M.; Poltavsky, I.; Schütt, K. T.; Tkatchenko, A.; Müller, K.-R. Machine learning force fields. *Chem. Rev.* **2021**, *121*, 10142–10186.
- (7) Merchant, A.; Batzner, S.; Schoenholz, S. S.; Aykol, M.; Cheon, G.; Cubuk, E. D. Scaling deep learning for materials discovery. *Nature* **2023**, *624*, 80–85.
- (8) Poltavsky, I.; Tkatchenko, A. Machine Learning Force Fields: Recent Advances and Remaining Challenges. *J. Phys. Chem. Lett.* **2021**, *12*, 6551–6564.

- (9) Smith, J. S.; Isayev, O.; Roitberg, A. E. ANI-1: an extensible neural network potential with DFT accuracy at force field computational cost. *Chem. Sci.* **2017**, *8*, 3192–3203.
- (10) Smith, J. S.; Nebgen, B. T.; Zubatyuk, R.; Lubbers, N.; Devereux, C.; Barros, K.; Tretiak, S.; Isayev, O.; Roitberg, A. E. Approaching coupled cluster accuracy with a general-purpose neural network potential through transfer learning. *Nat. Commun.* **2019**, *10*, 2903.
- (11) Devereux, C.; Smith, J. S.; Huddleston, K. K.; Barros, K.; Zubatyuk, R.; Isayev, O.; Roitberg, A. E. Extending the applicability of the ANI deep learning molecular potential to sulfur and halogens. *J. Chem. Theory Comput.* **2020**, *16*, 4192–4202.
- (12) Zheng, P.; Zubatyuk, R.; Wu, W.; Isayev, O.; Dral, P. O. Artificial intelligence-enhanced quantum chemical method with broad applicability. *Nat. Commun.* **2021**, *12*, 7022.
- (13) Qiao, Z.; Welborn, M.; Anandkumar, A.; Manby, F. R.; Miller III, T. F. OrbNet: Deep learning for quantum chemistry using symmetry-adapted atomic-orbital features. *J. Chem. Phys.* **2020**, *153*, 124111.
- (14) Christensen, A. S.; Sirumalla, S. K.; Qiao, Z.; O’Connor, M. B.; Smith, D. G.; Ding, F.; Bygrave, P. J.; Anandkumar, A.; Welborn, M.; Manby, F. R.; Miller III, T. F. OrbNet Denali: A machine learning potential for biological and organic chemistry with semi-empirical cost and DFT accuracy. *J. Chem. Phys.* **2021**, *155*, 204103.
- (15) Qiao, Z.; Christensen, A. S.; Welborn, M.; Manby, F. R.; Anandkumar, A.; Miller, T. F. Informing geometric deep learning with electronic interactions to accelerate quantum chemistry. *Proc. Natl. Acad. Sci. U. S. A.* **2022**, *119*, e2205221119.
- (16) Qiao, Z.; Ding, F.; Welborn, M.; Bygrave, P. J.; Smith, D. G.; Anandkumar, A.; Manby, F. R.; Miller III, T. F. Multi-task learning for electronic structure to predict and explore molecular potential energy surfaces. *arXiv [Preprint]* **2020**, <https://doi.org/10.48550/arXiv.2011.02680>.

- (17) Schütt, K.; Unke, O.; Gastegger, M. Equivariant message passing for the prediction of tensorial properties and molecular spectra. *arXiv [Preprint]* **2021**, <https://arxiv.org/abs/2102.03150>.
- (18) Ramakrishnan, R.; Dral, P. O.; Rupp, M.; Von Lilienfeld, O. A. Quantum chemistry structures and properties of 134 kilo molecules. *Sci. Data.* **2014**, *1*, 1–7.
- (19) Eastman, P.; Behara, P. K.; Dotson, D. L.; Galvelis, R.; Herr, J. E.; Horton, J. T.; Mao, Y.; Chodera, J. D.; Pritchard, B. P.; Wang, Y.; De Fabritiis, G.; Markland, T. P. SPICE, a dataset of drug-like molecules and peptides for training machine learning potentials. *Sci. Data.* **2023**, *10*, 11.
- (20) Bannwarth, C.; Ehlert, S.; Grimme, S. GFN2-xTB—An accurate and broadly parametrized self-consistent tight-binding quantum chemical method with multipole electrostatics and density-dependent dispersion contributions. *J. Chem. Theory Comput.* **2019**, *15*, 1652–1671.
- (21) Reiser, P.; Neubert, M.; Eberhard, A.; Torresi, L.; Zhou, C.; Shao, C.; Metni, H.; van Hoesel, C.; Schopmans, H.; Sommer, T.; Friederich, P. Graph neural networks for materials science and chemistry. *Commun. Mater.* **2022**, *3*, 93.
- (22) Thomas, N.; Smidt, T.; Kearnes, S.; Yang, L.; Li, L.; Kohlhoff, K.; Riley, P. Tensor field networks: Rotation-and translation-equivariant neural networks for 3d point clouds. *arXiv [Preprint]* **2018**, <https://arxiv.org/abs/1802.08219>.
- (23) Batzner, S.; Musaelian, A.; Sun, L.; Geiger, M.; Mailoa, J. P.; Kornbluth, M.; Molinari, N.; Smidt, T. E.; Kozinsky, B. E(3)-equivariant graph neural networks for data-efficient and accurate interatomic potentials. *Nat. Commun.* **2022**, *13*, 2453.
- (24) Geiger, M.; Smidt, T. e3nn: Euclidean Neural Networks. *arXiv [Preprint]* **2022**, <https://arxiv.org/abs/2207.09453>.

- (25) Liao, Y.-L.; Smidt, T. Equiformer: Equivariant graph attention transformer for 3D atomistic graphs. *arXiv [Preprint]* **2023**, <https://doi.org/10.48550/arXiv.2206.11990>.
- (26) Schütt, K. T.; Sauceda, H. E.; Kindermans, P.-J.; Tkatchenko, A.; Müller, K.-R. SchNet – A deep learning architecture for molecules and materials. *J. Chem. Phys.* **2018**, *148*, 241722.
- (27) Gasteiger, J.; Giri, S.; Margraf, J. T.; Günnemann, S. Fast and uncertainty-aware directional message passing for non-equilibrium molecules. *arXiv [Preprint]* **2020**, <https://doi.org/10.48550/arXiv.2011.14115>.
- (28) Simeon, G.; Fabritiis, G. D. TensorNet: Cartesian Tensor Representations for Efficient Learning of Molecular Potentials. *arXiv [Preprint]* **2023**, <https://doi.org/10.48550/arXiv.2306.06482>.
- (29) Ramakrishnan, R.; Dral, P. O.; Rupp, M.; Von Lilienfeld, O. A. Big data meets quantum chemistry approximations: the Δ -machine learning approach. *J. Chem. Theory Comput.* **2015**, *11*, 2087–2096.
- (30) Wu, J.; Xu, X. The X1 method for accurate and efficient prediction of heats of formation. *J. Chem. Phys.* **2007**, *127*, 214105.
- (31) Zhang, I. Y.; Wu, J.; Xu, X. Extending the reliability and applicability of B3LYP. *Chem. Commun.* **2010**, *46*, 3057–3070.
- (32) Zhou, Y.; Wu, J.; Xu, X. Improving B3LYP heats of formation with three-dimensional molecular descriptors. *J. Comput. Chem.* **2016**, *37*, 1175–1190.
- (33) Christensen, A. S.; Kubar, T.; Cui, Q.; Elstner, M. Semiempirical quantum mechanical methods for noncovalent interactions for chemical and biochemical applications. *Chem. Rev.* **2016**, *116*, 5301–5337.

- (34) Dral, P. O.; Hourahine, B.; Grimme, S. Modern semiempirical electronic structure methods. *J. Chem. Phys.* **2024**, *160*, 040401.
- (35) Wengert, S.; Csányi, G.; Reuter, K.; Margraf, J. T. A Hybrid Machine Learning Approach for Structure Stability Prediction in Molecular Co-crystal Screenings. *J. Chem. Theory Comput.* **2022**, *18*, 4586–4593.
- (36) Fan, G.; McSloy, A.; Aradi, B.; Yam, C.-Y.; Frauenheim, T. Obtaining electronic properties of molecules through combining density functional tight binding with machine learning. *J. Phys. Chem. Lett.* **2022**, *13*, 10132–10139.
- (37) Behler, J.; Parrinello, M. Generalized neural-network representation of high-dimensional potential-energy surfaces. *Phys. Rev. Lett.* **2007**, *98*, 146401.
- (38) Welborn, M.; Cheng, L.; Miller III, T. F. Transferability in machine learning for electronic structure via the molecular orbital basis. *J. Chem. Theory Comput.* **2018**, *14*, 4772–4779.
- (39) Cheng, L.; Welborn, M.; Christensen, A. S.; Miller III, T. F. A universal density matrix functional from molecular orbital-based machine learning: Transferability across organic molecules. *J. Chem. Phys.* **2019**, *150*, 131103.
- (40) Cheng, L.; Sun, J.; Deustua, J. E.; Bhethanabotla, V. C.; Miller III, T. F. Molecular-orbital-based machine learning for open-shell and multi-reference systems with kernel addition Gaussian process regression. *J. Chem. Phys.* **2022**, *157*, 154105.
- (41) Smith, J. S.; Zubatyuk, R.; Nebgen, B.; Lubbers, N.; Barros, K.; Roitberg, A. E.; Isayev, O.; Tretiak, S. The ANI-1ccx and ANI-1x data sets, coupled-cluster and density functional theory properties for molecules. *Sci Data* **2020**, *7*, 134.
- (42) Mardirossian, N.; Head-Gordon, M. ω B97M-V: A combinatorially optimized, range-

- separated hybrid, meta-GGA density functional with VV10 nonlocal correlation. *J. Chem. Phys.* **2016**, *144*, 214110.
- (43) Najibi, A.; Goerigk, L. The nonlocal kernel in van der Waals density functionals as an additive correction: An extensive analysis with special emphasis on the B97M-V and ω B97M-V approaches. *J. Chem. Theory Comput.* **2018**, *14*, 5725–5738.
- (44) Grimme, S.; Bannwarth, C.; Shushkov, P. A robust and accurate tight-binding quantum chemical method for structures, vibrational frequencies, and noncovalent interactions of large molecular systems parametrized for all spd-block elements (Z= 1–86). *J. Chem. Theory Comput.* **2017**, *13*, 1989–2009.
- (45) Dral, P. O.; Wu, X.; Thiel, W. Semiempirical quantum-chemical methods with orthogonalization and dispersion corrections. *J. Chem. Theory Comput.* **2019**, *15*, 1743–1760.
- (46) Lin, Y.-S.; Li, G.-D.; Mao, S.-P.; Chai, J.-D. Long-Range Corrected Hybrid Density Functionals with Improved Dispersion Corrections. *J. Chem. Theory Comput.* **2013**, *9*, 263–272.
- (47) Goerigk, L.; Hansen, A.; Bauer, C.; Ehrlich, S.; Najibi, A.; Grimme, S. A look at the density functional theory zoo with the advanced GMTKN55 database for general main group thermochemistry, kinetics and noncovalent interactions. *Phys. Chem. Chem. Phys.* **2017**, *19*, 32184–32215.
- (48) Chen, Y.; Ou, Y.; Zheng, P.; Huang, Y.; Ge, F.; Dral, P. O. Benchmark of general-purpose machine learning-based quantum mechanical method AIQM1 on reaction barrier heights. *J. Chem. Phys.* **2023**, *158*, 074103.
- (49) Prasad, V. K.; Pei, Z.; Edelmann, S.; Otero-de-la Roza, A.; DiLabio, G. A. BH9, a new comprehensive benchmark data set for barrier heights and reaction energies: Assessment of density functional approximations and basis set incompleteness potentials. *J. Chem. Theory Comput.* **2021**, *18*, 151–166.

- (50) Rezáč, J.; Riley, K. E.; Hobza, P. S66: A well-balanced database of benchmark interaction energies relevant to biomolecular structures. *J. Chem. Theory Comput.* **2011**, *7*, 2427–2438.
- (51) Sellers, B. D.; James, N. C.; Gobbi, A. A comparison of quantum and molecular mechanical methods to estimate strain energy in druglike fragments. *J. Chem. Inf. Model.* **2017**, *57*, 1265–1275.
- (52) Risthaus, T.; Steinmetz, M.; Grimme, S. Implementation of nuclear gradients of range-separated hybrid density functionals and benchmarking on rotational constants for organic molecules. *J. Comput. Chem.* **2014**, *35*, 1509–1516.
- (53) Maurer, M.; Ochsenfeld, C. Spin Component-Scaled Second-Order Møller–Plesset Perturbation Theory for Calculating NMR Shieldings. *Journal of Chemical Theory and Computation* **2015**, *11*, 37–44.
- (54) Bursch, M.; Mewes, J.-M.; Hansen, A.; Grimme, S. Best-Practice DFT Protocols for Basic Molecular Computational Chemistry. *Angew. Chem. Int. Ed.* **2022**, *61*, e202205735.
- (55) Pollack, S. K.; Raine, B. C.; Hehre, W. J. Determination of the heats of formation of the isomeric xylylenes by ion cyclotron double-resonance spectroscopy. *J. Am. Chem. Soc.* **1981**, *103*, 6308–6313.
- (56) Keiichi, N.; Ninoru, S.; Syûzô, S.; Hisanori, H.; Tetsuo, O.; Soichi, M. Thermochemical studies on double- and triple-layered [2.2] paracyclophanes. Estimation of molecular strain energies. *Bull. Chem. Soc. Jpn.* **1980**, *53*, 869–877.
- (57) Shieh, C.-F.; McNally, D.; Boyd, R. The heats of combustion and strain energies of some cyclophanes. *Tetrahedron* **1969**, *25*, 3653–3665.
- (58) Inagaki, S.; Murata, S.; Sakiyama, M.; Ito, Y.; Umehara, Y.; Hijiya, T.; Matsuura, T. Thermochemical studies on 2, 4, 6-triisopropylbenzophenone and its photo-isomer, 3', 5'-

- diisopropyl-4, 4-dimethyl-3-phenyl-1, 2-benzocyclobuten-3-ol. Evaluation of magnitude of light energy stored in the latter molecule. *Bull. Chem. Soc. Jpn.* **1982**, *55*, 2803–2807.
- (59) Zubatyuk, R.; Smith, J. S.; Nebgen, B. T.; Tretiak, S.; Isayev, O. Teaching a neural network to attach and detach electrons from molecules. *Nat. Commun.* **2021**, *12*, 4870.
- (60) Unke, O. T.; Chmiela, S.; Gastegger, M.; Schütt, K. T.; Sauceda, H. E.; Müller, K.-R. SpookyNet: Learning force fields with electronic degrees of freedom and nonlocal effects. *Nat. Commun.* **2021**, *12*, 7273.
- (61) Guan, X.; Heindel, J. P.; Ko, T.; Yang, C.; Head-Gordon, T. Using machine learning to go beyond potential energy surface benchmarking for chemical reactivity. *Nat. Comput. Sci.* **2023**, *3*, 965–974.
- (62) Paszke, A. et al. PyTorch: An Imperative Style, High-Performance Deep Learning Library. *arXiv [Preprint]* **2019**, <https://doi.org/10.48550/arXiv.1912.01703>.
- (63) Fey, M.; Lenssen, J. E. Fast Graph Representation Learning with PyTorch Geometric. 2019; https://github.com/pyg-team/pytorch_geometric.
- (64) Geiger, M. et al. Euclidean neural networks: e3nn. 2022; <https://doi.org/10.5281/zenodo.6459381>.
- (65) Tang, Z.; Ehlert, S.; Friede, M.; Karandashev, K. Light-weight tight-binding framework. 2022; <https://github.com/tblite/tblite>, <https://github.com/tblite/tblite>.
- (66) Wang, L.-P.; Song, C. Geometry optimization made simple with translation and rotation coordinates. *J. Chem. Phys.* **2016**, *144*, 214108.
- (67) Sun, Q. et al. Recent developments in the PySCF program package. *J. Chem. Phys.* **2020**, *153*, 024109.
- (68) Neese, F. Software update: The ORCA program system—Version 5.0. *WIREs Comput. Mol. Sci.* **2022**, *12*, e1606.

- (69) Dral, P. O.; Ge, F.; Xue, B.-X.; Hou, Y.-F.; Pinheiro Jr, M.; Huang, J.; Barbatti, M. MLatom 2: An Integrative Platform for Atomistic Machine Learning. *Top. Curr. Chem.* **2021**, *379*, 27.
- (70) Bannwarth, C.; Caldeweyher, E.; Ehlert, S.; Hansen, A.; Pracht, P.; Seibert, J.; Spicher, S.; Grimme, S. Extended tight-binding quantum chemistry methods. *WIREs Comput. Mol. Sci.* **2021**, *11*, e1493.
- (71) Smith, D. G. A.; Burns, L. A.; Patkowski, K.; Sherrill, C. D. Revised Damping Parameters for the D3 Dispersion Correction to Density Functional Theory. *J. Phys. Chem. Lett.* **2016**, *7*, 2197–2203.
- (72) Thiel, W.; Beck, M.; Billeter, S.; Kevorkiants, R.; Kolb, M.; Koslowski, A.; Patchkovskii, S.; Turner, A.; E.-U., W.; Weber, W.; Spörkel, L.; Dral, P. O. MNDO2020: a semiempirical quantum chemistry program. 2020; <https://mndo.kofo.mpg.de/>.

Supporting Information for Constructing accurate and efficient general-purpose atomistic machine learning model with transferable accuracy for quantum chemistry

Yicheng Chen,^{†,¶} Wenjie Yan,^{†,¶} Zhanfeng Wang,[†] Jianming Wu,^{*,†} and Xin Xu^{*,†,‡}

[†]*Collaborative Innovation Center of Chemistry for Energy Materials, Shanghai Key Laboratory of Molecular Catalysis and Innovative Materials, MOE Key Laboratory of Computational Physical Sciences, Department of Chemistry, Fudan University, 200433, Shanghai, People's Republic of China*

[‡]*Hefei National Laboratory, 230088, Hefei, People's Republic of China*

[¶]*These authors contribute equally.*

E-mail: jianmingwu@fudan.edu.cn; xxchem@fudan.edu.cn

Equivariant graph neural network

Atomistic systems can be represented as coordinate systems in 3D Euclidean space. Transformations that preserve Euclidean distance between any two points in 3D space form the group of $E(3)$. Specifically, this group encompasses three types of transformations: translation \hat{T} , rotation \hat{R} and inversion \hat{I} . Furthermore, \hat{T} and \hat{R} form the group $SE(3)$. $SO(3)$ group only considers rotation symmetry, while $O(3)$ group consists of \hat{R} and \hat{I} , which are subgroups of $E(3)$.^{1,2}

The conventional strategy of using relative position vectors $\{\vec{r}_{AB}\}$ in graph representation fulfills the translation equivariance for a Graph Neural Network (GNN) model. This equivariant GNN differs from the invariant model by further fulfilling rotation and inversion ($O(3)$ group) equivariance. As a result, GNNs enable the hidden feature and the output being transformed consistently alongside changes the input space.

$$\tilde{\mathcal{Y}} \equiv \mathcal{F}(\mathcal{R} \cdot \mathbf{x}) = \mathcal{R} \cdot \mathcal{F}(\mathbf{x}) \equiv \mathcal{R} \cdot \mathcal{Y}, \mathcal{R} \in \{\hat{R}, \hat{I}\} \quad (\text{S1})$$

Many equivariant models are $SE(3)$ -equivariant,^{2,3} where inversion operation \hat{I} is ignored. This is achieved via operating on geometric tensors χ in spherical representation consists of direct sum of irreducible representations (Irrep) $\omega^{(l)}$ of $SO(3)$ group by different angular momentum degree l . Models operating on geometric tensors in Cartesian form also exhibit $SE(3)$ -equivariance. Two examples PaiNN⁴ and TensorNet.⁵ PaiNN adopts separate scalar $\mathbf{s}(l=0)$ and vector $\mathbf{v}(l=1)$ feature channels, while TensorNet decomposes rank-2 tensor representation into diagonal ($l=0$), off-diagonal ($l=1$) and trace-less ($l=2$) part. These separations or decompositions allow the model to handle different types of interactions and symmetries effectively.

In the current work, the XPaiNN architecture is also $SE(3)$ -equivariant.

Model Details

Detailed Architecture

Node Embedding. A well-recognized weakness of the ANI potentials⁶ is their inability to predict properties of chemical compounds that contain elements not present in the dataset used for model training. Thus, introducing a new type of element requires a bottom-up reconstruction of the model.⁷ GNNs avoid this defect via element-wise node embedding. However, the widely used embedding for atoms in GNN is one-hot encoding, which cannot ensure reasonable inference results for the aforementioned situations, as it fails to reflect the chemical relations as dictated by the periodic table law of elements. By contrast, OrbNet^{8,9} utilizes diagonal blocks of matrices from quantum mechanics (QM) calculations as node embedding feature, which empowers the model to adeptly manage compounds composed of untrained elements.

Drawing inspiration from the strengths of OrbNet and recognizing that its superiority partly stems from the application of specific basis sets in QM calculations, we come up with the design of the node embedding scalar feature by projecting element-wise atomic orbital basis sets onto a uniform set of auxiliary basis. By doing so, we create features that vary periodically, akin to the element properties across the periodic table, while also maintaining a consistent dimensionality. This ensures that our features can be uniformly applied and compared, regardless of the specific element under consideration, thereby enriching the representational capacity of our model.

We first define a set of Gaussian-type auxiliary basis functions $\tilde{\Phi}_{n,l,m}$:

$$\tilde{\Phi}_{n,l,m}(\mathbf{r}) := A_{n,l} \cdot r^l \exp(-\alpha_{n,l} r^2) \mathcal{Y}_{l,m}(\hat{\mathbf{r}}) \quad (\text{S2})$$

where $r = \|\mathbf{r}\|$, $\hat{\mathbf{r}} = \mathbf{r}/r$, $\mathcal{Y}_{l,m}(\cdot)$ is the real spherical harmonics for given angular and magnetic quantum numbers l and m , and $A_{n,l}$ is the normalization factor where n is the principle

quantum number. In Eq. (S2), the scaling parameters $\alpha_{n,l}$ are pre-determined for different n and l as:

$$\begin{cases} \alpha_{n,0} := 128 \cdot \left(\frac{1}{\sqrt{2}}\right)^{n-1} & \text{where } n \in \{1, 2, \dots, 32\} \\ \alpha_{n,1} := 64 \cdot \left(\frac{1}{2}\right)^{n-1} & \text{where } n \in \{1, 2, \dots, 16\} \\ \alpha_{n,2} := 4 \cdot \left(\frac{1}{2}\right)^{n-1} & \text{where } n \in \{1, 2, \dots, 8\} \end{cases} \quad (\text{S3})$$

Afterwards, we employ the valence basis sets of GFN2-xTB¹⁰ as the atomic orbital basis function $\Psi_{n,l,m}^{Z_A}$ with each element type A described by the nuclear charge number Z_A . Then, element-wise features are computed as the overlap integrals between the two sets of orbitals at the same coordinate origin.

$$(\mathbf{S}^{Z_A})_{\mu\nu} = S_{(n_1,l_1,0)(n_2,l_2,0)}^{Z_A} = \left\langle \tilde{\Phi}_{n_1,l_1,0} \left| \Psi_{n_2,l_2,0}^{Z_A} \right. \right\rangle \quad (\text{S4})$$

Note in Eq.(S4), we only calculate overlap integrals between orbitals with $m = 0$, while there is no need to calculate overlap integrals between orbitals of different m due to orthogonality. Finally, the embedding feature \mathbf{e}^{Z_A} is obtained by sum over \mathbf{S}^{Z_A} along the atomic basis dimension ν

$$(\mathbf{e}^{Z_A})_{\mu} = \sum_{\nu} (\mathbf{S}^{Z_A})_{\mu\nu} \quad (\text{S5})$$

The above process generates \mathbf{e}^{Z_A} as an array of 56 dimensions for each element type A , which are visualized using the color scale as shown in Figure S1. Periodic changes in the atomic orbital basis result in the periodic changes in atom embedding vectors, which reflect the periodic table law of the elements to some extent.

Radial Basis Function (RBF). The interatomic distance r_{ij} is represented through an expansion using the 0-order spherical Bessel function of the first kind, a method same as that in DimeNet.¹¹ A number of RBFs are used to perform a filter-like action on the interatomic

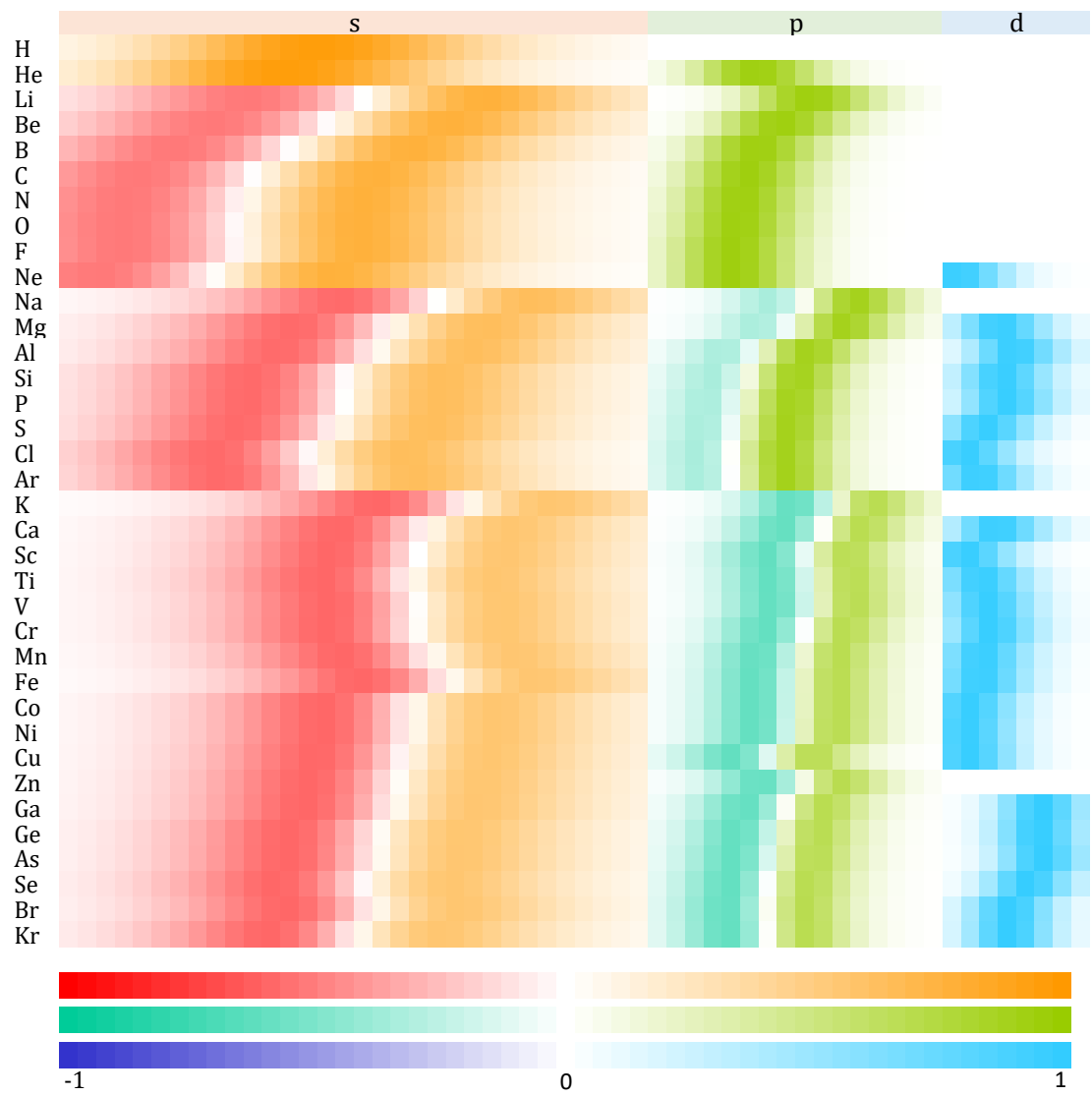


Figure S1: Visualization of atom embeddings. Color shades indicate embedding vector values.

distances, with the k -th function defined as

$$R_k(r_{ij}) = \sqrt{\frac{2}{c}} \frac{\sin(f_k r_{ij})}{r_{ij}} \quad (\text{S6})$$

where c is the cutoff radius and f_k is a trainable parameter initialized with $\frac{k\pi}{c}$. These RBFs are then linearly combined and smoothly truncated with cosine cutoff function.

$$\mathcal{W}_{ij} = \left[\sum_{k=1}^n w_k R_k(r_{ij}) + b \right] \cdot \frac{1}{2} \left[\cos\left(\pi \frac{r}{c}\right) + 1 \right] \quad (\text{S7})$$

Real Spherical Harmonics (RSH). The relative orientations \hat{r}_{ij} between atoms are expanded using RSHs. The orientation information is then introduced into the network, forming the equivariant spherical tensors as:

$$\mathcal{Y}_{l,m}(\hat{r}_{ij}) = \begin{cases} \frac{1}{\sqrt{2}} [Y_{l,-m}(\hat{r}_{ij}) + (-1)^m Y_{l,m}(\hat{r}_{ij})] & \text{if } m > 0 \\ Y_{l,0}(\hat{r}_{ij}) & \text{if } m = 0 \\ \frac{1}{\sqrt{2i}} [Y_{l,m}(\hat{r}_{ij}) - (-1)^m Y_{l,-m}(\hat{r}_{ij})] & \text{if } m < 0 \end{cases} \quad (\text{S8})$$

$$Y_{l,m}(\hat{r}_{ij}) = Y_{l,m}(\theta, \phi) = \sqrt{\frac{2l+1}{4\pi} \frac{(l-m)!}{(l+m)!}} P_l^m(\cos\theta) e^{im\phi} \quad (\text{S9})$$

$Y_{l,m}(\cdot)$ is the complex spherical harmonics and $\mathcal{Y}_{l,m}(\cdot)$ is the desired RSHs.

Spherical Tensor. Spherical Tensor serves as the basic data structure for $E(3)$ equivariant operations on tensor data. It is characterized by a direct sum of inequivalent irreducible representations of $E(3)$ group (Irreps), combined with numbers indicating feature channels in each tensor of l order.¹ The schematic is illustrated in Figure S2.

$O(3)$ Linear. Linear transformations are separately carried out for each tensor of l order $\omega^{(l,p)}$ in Irreps to ensure equivariance. In this framework, the number of channels is adjustable. Notably, the bias term can only be incorporated into the transformation for the

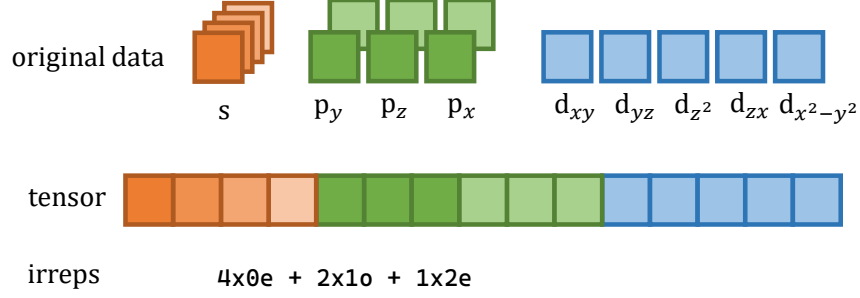


Figure S2: Schematic of Spherical Tensor

0th order Irrep (i.e. the scalar-type) for $l = 0$,

$$[O(3)\text{Linear}(\boldsymbol{\chi})]_{l,p} = \begin{cases} \boldsymbol{\omega}^{(l,p)} \mathbf{W}_{l,p}^\top + \mathbf{b}_p & l = 0 \\ \boldsymbol{\omega}^{(l,p)} \mathbf{W}_{l,p}^\top & l > 0 \end{cases} \quad (\text{S10})$$

where p denotes the parity, which refers to the inversion symmetry. The schematic is shown in Figure S3.

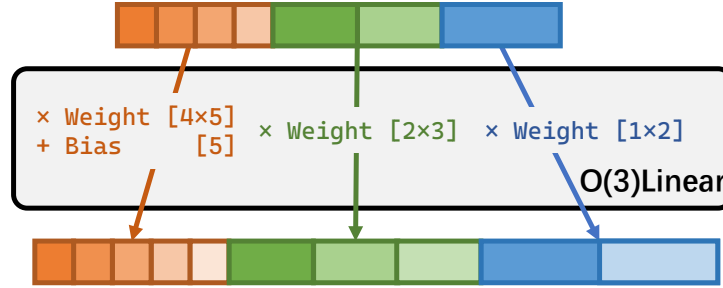


Figure S3: Schematic of $O(3)$ linear transform.

$O(3)$ Inner Product. To compute the inner product of two spherical tensors of the same layout, one performs element-wise multiplication and sum over the degenerate dimension, represented by m , for each distinct value of l .

$$\boldsymbol{\chi}_1 \odot \boldsymbol{\chi}_2 = \bigoplus_{l,p} \boldsymbol{\omega}_1^{(l,p)} \cdot \boldsymbol{\omega}_2^{(l,p)} \quad (\text{S11})$$

$$\boldsymbol{\omega}_1 \cdot \boldsymbol{\omega}_2 = \sum_{m=-l}^l (\boldsymbol{\omega}_1)_m (\boldsymbol{\omega}_2)_m \quad (\text{S12})$$

For simplification, (l, p) is omitted for $\boldsymbol{\omega}$ in Eq. S12. The result is a scalar tensor, as shown in Figure S4

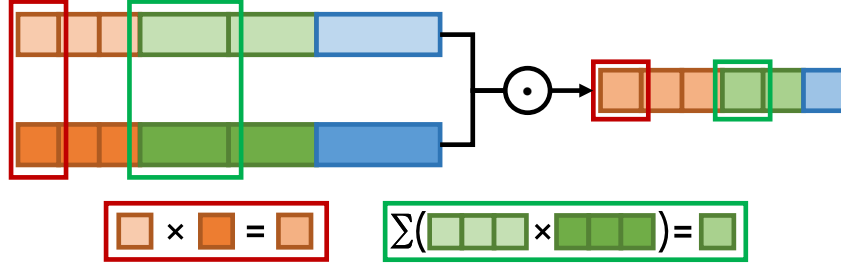


Figure S4: Schematic of inner product between two spherical tensors.

Invariant. Similar to **$O(3)$ Inner Product**, one computes the L2-norm of each $\boldsymbol{\omega}^{(l,p)}$ as shown in Figure S5 . The result is also a scalar tensor.

$$\|\boldsymbol{\chi}\| = \bigoplus_{l,p} \sqrt{\sum_{m=-l}^l |(\boldsymbol{\omega}_m)|^2} \quad (\text{S13})$$

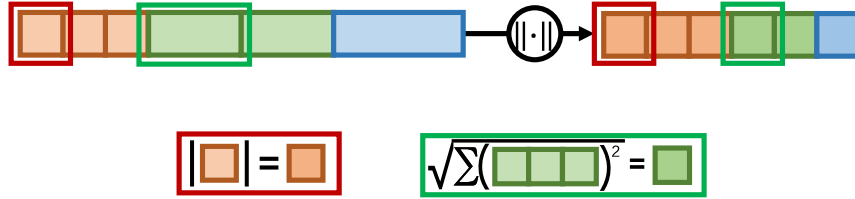


Figure S5: Schematic of invariant operation on a spherical tensor.

Hadamard Product. A Hadamard product can be computed between a spherical tensor and a scalar tensor, provided that the length of the scalar tensor is the same as the number of Irreps channel in the spherical tensor, as illustrated in Figure S6. In this context, $\boldsymbol{\omega}^{(l,p)}$ is multiplied, term by term, by the value of the corresponding scalar tensor.

$$(\boldsymbol{\chi} \circ \mathbf{x})_{l,m,p} = (\boldsymbol{\chi})_{l,m,p} (\mathbf{x})_{l,p} \quad (\text{S14})$$

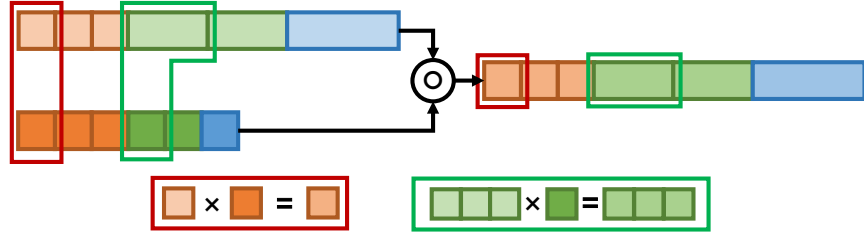


Figure S6: Schematic of Hadamard product between a spherical tensor and a scalar tensor.

$O(3)$ Normalization. The equivariant normalization is done by deducting the mean for scalar sub-tensor, and dividing the overall spherical tensor by the root mean square of its invariant tensor as shown in Figure S7. Note, the "+" and "-" is performed only for the 0th order Irreps.

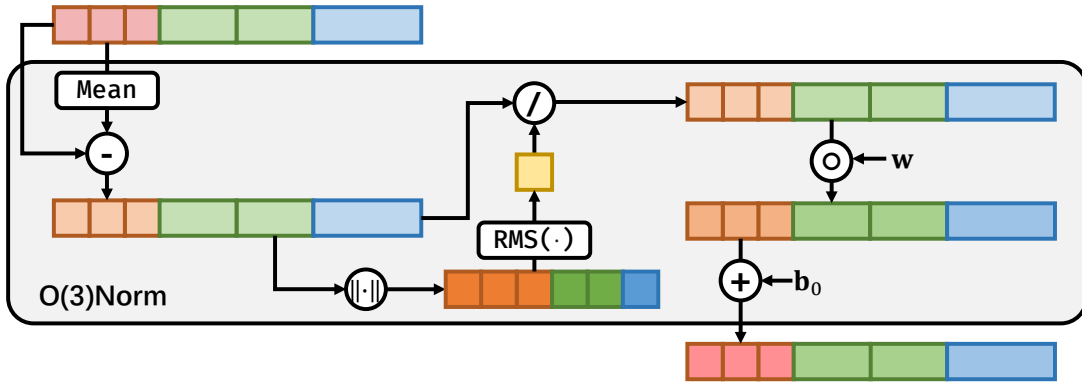


Figure S7: Schematic of the layer normalization of a spherical tensor.

order Irreps. w and b_0 are parameters to be optimized. $\text{RMS}(\cdot)$ refers to root mean square.

Activation Gate. The activation gate for spherical tensor is constructed based on the sigmoid linear unit (SiLU) activation function as shown in Figure S8.

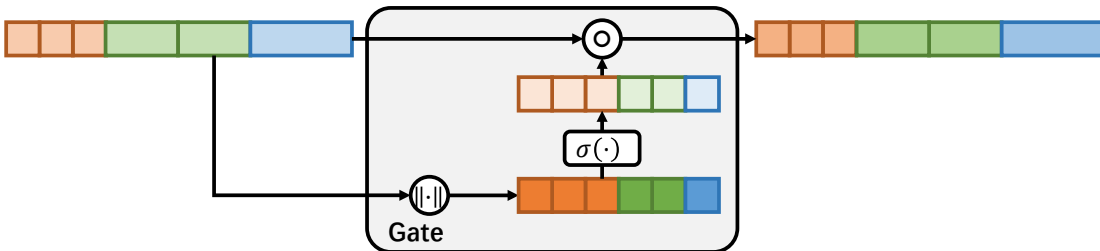


Figure S8: Schematic of activation gate of a spherical tensor.

$$\text{SiLU}(x) = x * \sigma(x) \quad (\text{S15})$$

$$\text{Gate}(\chi) = \chi \circ \sigma(\|\chi\|) \quad (\text{S16})$$

Here, $\sigma(\cdot)$ is the sigmoid function, i.e. $\sigma(x) = (1 + e^{-x})^{-1}$.

Node updating

In the node updating layer depicted in Fig. S9, scalar and spherical features are coupled to update both, while the operations on spherical features are localized within each irreducible representation to ensure the equivariance.

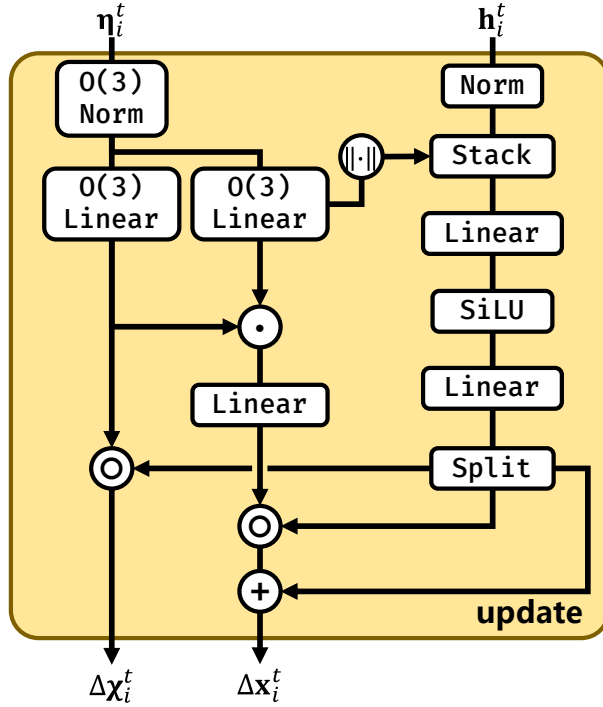


Figure S9: Schematic of node updating layer.

$$\mathbf{x}_i^t = \mathbf{h}_i^t + f_u^t(\mathbf{h}_i^t, \eta_i^t) \quad (\text{S17})$$

$$\chi_i^t = \eta_i^t + \phi_u^t(\mathbf{h}_i^t, \eta_i^t) \quad (\text{S18})$$

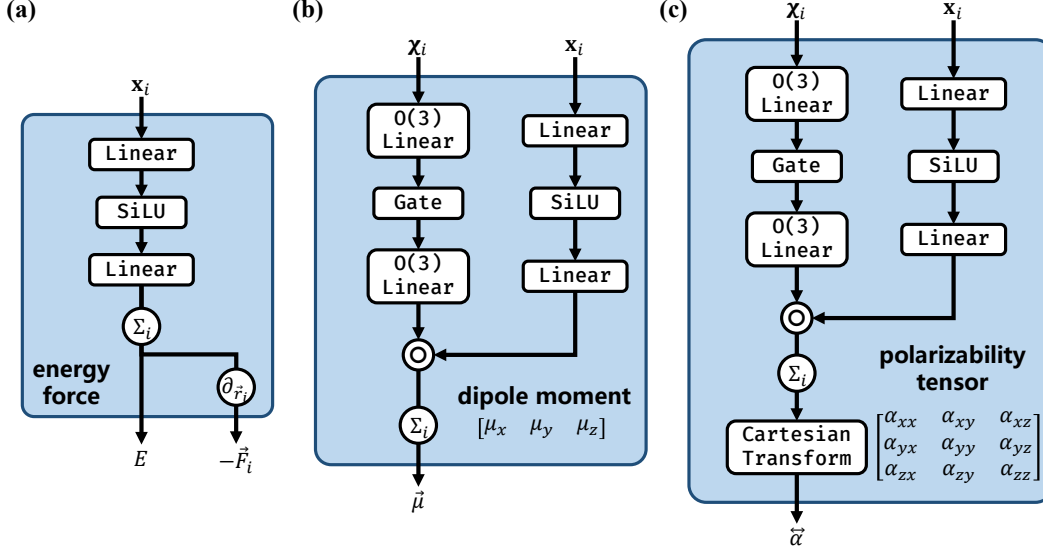


Figure S10: **Schematic diagram of output layers. Tensor dimensions and irreducible representations are shown in grey.** (a) Energy and gradient force output. (b) Dipole moment output. (c) Polarizability tensor output.

Output

The final output layer are designed according to the target property.

Energy, a scalar property, can be constructed through scalar features (Figure S10(a)).

Force, an atom-wise feature, is obtained by taking derivative of the energy with respect to the coordinates.

$$E = \sum_i f_o^E(\mathbf{x}_i), \quad \vec{F}_A = -\frac{\partial E}{\partial \mathbf{r}_A} \quad (\text{S19})$$

Dipole moment, a vector feature, is derived from the p-type part of spherical features (Figure S10(b))

$$\vec{\mu} = (\mu_x, \mu_y, \mu_z) = \sum_i \phi_o^\mu(\mathbf{x}_i, \chi_i) \quad (\text{S20})$$

The modulus of dipole moment is calculated as

$$\mu = \|\vec{\mu}\| = \sqrt{\mu_x^2 + \mu_y^2 + \mu_z^2} \quad (\text{S21})$$

Polarizability tensor, a symmetric order-2 tensor, has six degrees of freedom. Therefore,

the output in spherical representation is $1 \times 0e + 1 \times 2e$. (Figure S10(c)).

$$(\alpha_0, \alpha_{xy}, \alpha_{yz}, \alpha_{z^2}, \alpha_{zx}, \alpha_{x^2-y^2}) = \sum_i \phi_o^\alpha(\mathbf{x}_i, \boldsymbol{\chi}_i) \quad (\text{S22})$$

In the output layer, the model's hidden features are first transformed into the required spherical representation. Subsequently, features of the second-order spherical harmonic type are further converted into the Cartesian form.

$$\begin{aligned} |\alpha| &= \sqrt{\alpha_{xy}^2 + \alpha_{yz}^2 + \alpha_{z^2}^2 + \alpha_{zx}^2 + \alpha_{x^2-y^2}^2} \\ \alpha_{xx} &= \frac{1}{\sqrt{3}} (|\alpha| - \alpha_{z^2}) + \alpha_{x^2-y^2} \\ \alpha_{yy} &= \frac{1}{\sqrt{3}} (|\alpha| - \alpha_{z^2}) - \alpha_{x^2-y^2} \\ \alpha_{zz} &= \frac{1}{\sqrt{3}} (|\alpha| + 2\alpha_{z^2}) \\ \alpha_{xy} &= \alpha_{yx} \quad \alpha_{yz} = \alpha_{zy} \quad \alpha_{zx} = \alpha_{xz} \end{aligned} \quad (\text{S23})$$

The polarizability tensor is then written in the form of a 3×3 matrix and α_0 is added to each diagonal element.

$$\overleftrightarrow{\alpha} = \begin{pmatrix} \alpha_{xx} & \alpha_{xy} & \alpha_{xz} \\ \alpha_{yx} & \alpha_{yy} & \alpha_{yz} \\ \alpha_{yz} & \alpha_{zy} & \alpha_{zz} \end{pmatrix} + \begin{pmatrix} \alpha_0 & 0 & 0 \\ 0 & \alpha_0 & 0 \\ 0 & 0 & \alpha_0 \end{pmatrix} \quad (\text{S24})$$

The isotropic polarizability is obtained by calculating the trace of $\overleftrightarrow{\alpha}$

$$\alpha = \frac{1}{3} \text{tr}(\overleftrightarrow{\alpha}) \quad (\text{S25})$$

Electronic spatial extent, for a mass-centered molecule, can be obtained from the following equation.

$$\langle R^2 \rangle = \sum_i \|\mathbf{r}_i\|^2 f_o^R(\mathbf{x}_i) \quad (\text{S26})$$

Architecture Comparison

The main differences between XPaiNN and the original PaiNN lie in the embedding type and the form of equivariant features, which are illustrated in Fig S11. As for the embedding type, XPaiNN uses a method of orbital projection as described in **Detailed Architecture**, whereas PaiNN simply uses one-hot encoding and linear transformation to derive the initial invariant features. As for equivariant features, XPaiNN expands the relative positions of atom pairs with real spherical harmonics to obtain Irreps of different angular momentum to form equivariant features, while PaiNN only uses unit vectors of relative positions as equivariant features, which is literally the Irrep with angular momentum of $l = 1$. As a result, the corresponding layers in XPaiNN are adapted to accommodate the $O(3)$ group. In addition, XPaiNN incorporates normalization layers, which enhances the gradient flow and training stability.

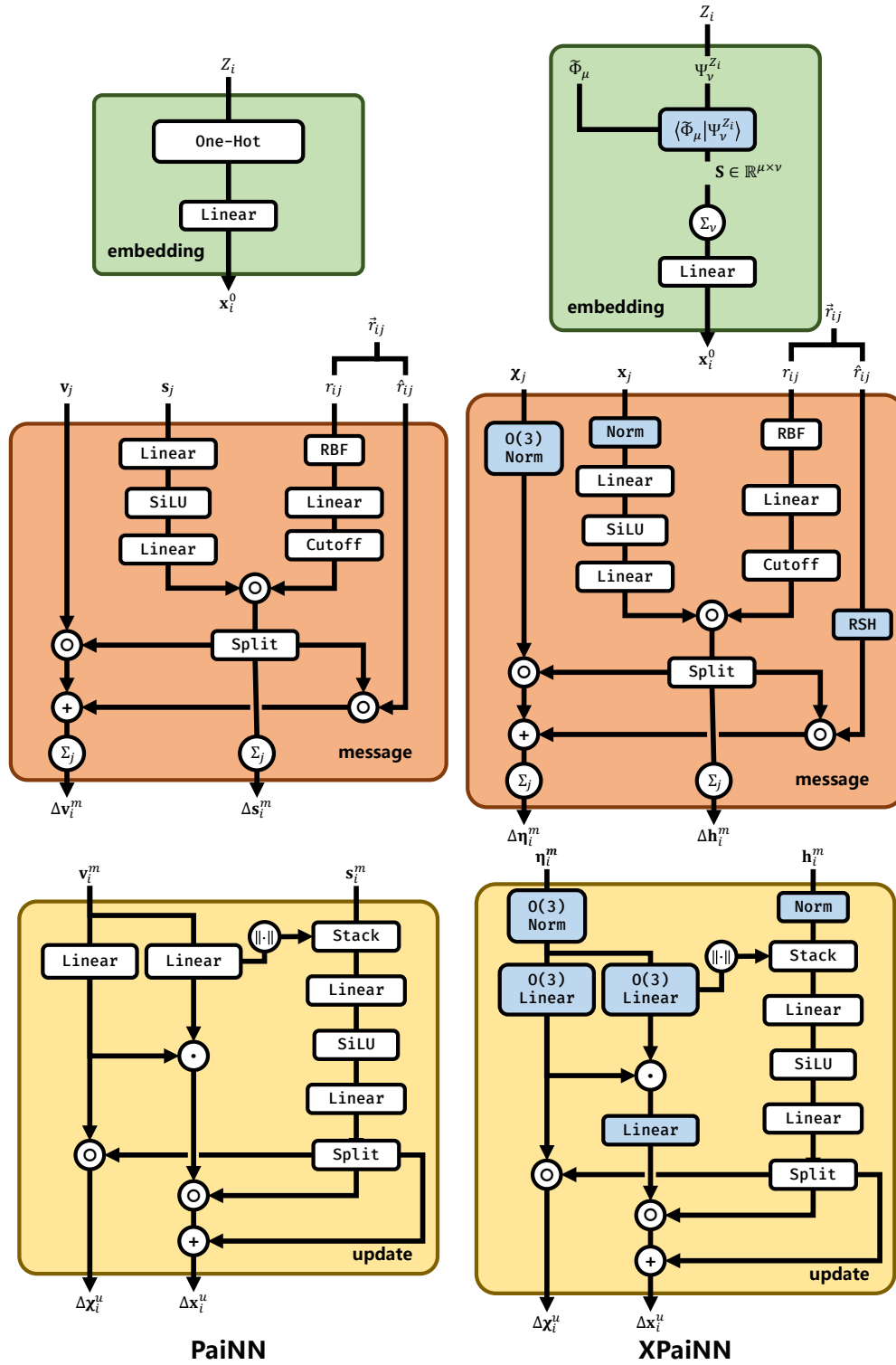


Figure S11: Comparison of the model architecture between original PaiNN and XPaiNN. The modification parts are marked as blue blocks.

Training Details

QM9. For all 12 tasks in QM9, we employ the same partition strategy, which randomly divide the dataset into three parts (110k, 10k and 11k) for training, validation and testing, respectively. For each distinct task, individual models are trained with the same hyper-parameters summarized in Table S1, with the exception of the **Output hidden Irreps** parameters, which are tailored to match the target properties as depicted in **Output**. For $\langle R^2 \rangle$ task, we use the same output as PaiNN,⁴ calculated according to Eq. S26. For certain tasks, a linear fitting based on element type towards the training set labels is performed. The as-obtained results are then subtracted from the training labels, which are subsequently reinstated during testing to refine predictions. For Δ -learning tasks of U_0 , U , H and G , we subtract the energies of each isolated atom calculated at the respective label and baseline methods to ensure the consistency. Training for each property in QM9 was conducted using a single NVIDIA RTX2080 Ti graphics processing unit (GPU) card.

Table S1: Hyper-parameters for training QM9 tasks.

Hyper-parameters	Value or description
Scalar feature dimension	128
Spherical feature Irreps	128x0e+64x1o+32x2e
Output hidden dimension	64
Output hidden Irreps	32x1o for μ , 64x0e+16x2e for α
Number of radius basis	20
Cutoff radius (Å)	5.0
Layer normalization	False
Number of interaction blocks	3
Batch size	100
Training epochs	2500
Learning rate warmup	Linear warmup for 10 epochs
Maximum learning rate	5×10^{-4}
Learning rate scheduler	Cosine annealing with Tmax=500 epochs
Loss function	Smooth L1
Optimizer	Adam
Exponential moving average decay	0.995
Total number of parameters	861k

MD17 and rMD17. For training and validation, we randomly select 950 and 50 different configurations, respectively, and we use the remaining configurations for test. Model hyper-parameters are summarized in Table S2. We subtract the energies of isolated atoms at the same level of the label for training, and we use the averaged energy as the initial bias for the linear layer in the output module. Training for each molecule is conducted on a single NVIDIA RTX2080 Ti GPU card.

Table S2: Hyper-parameters for MD17 and rMD17 dataset.

Hyper-parameters	Value or description
Scalar feature dimension	128
Spherical feature Irreps	128x0e+64x1o+32x2e
Output hidden dimension	64
Number of radius basis	20
Cutoff radius (Å)	5.0
Layer normalization	False
Number of interaction blocks	3
Batch size	10
Training epochs	2500
Learning rate warmup	Linear warmup for 10 epochs
Maximum learning rate	5×10^{-4}
Learning rate scheduler	Cosine annealing with Tmax=500 epochs
Loss function	MSE Loss
Loss ratio of energy and force	1:99
Optimizer	Adam
Exponential moving average decay	0.995
Total number of parameters	861k

SPICE. The training set used for constructing the general models is selected from 3 subsets in SPICE, namely PubChem, DES370K Monomers and DES370K Dimers, covering elements of H, C, N, O, F, P, S, Cl, Br and I. Systems that are not neutral or closed-shell are excluded from our selections. This results in a training set of nearly 1 million conformations, spanning over 18,000 organic and inorganic molecules.

Table S3: Hyper-parameters for the selected SPICE dataset.

Hyper-parameters	Value or description
Scalar feature dimension	128
Spherical feature Irreps	128x0e+64x1o+32x2e
Output hidden dimension	64
Number of radius basis	20
Cutoff radius (Å)	5.0
Layer normalization	True
Number of interaction blocks	3
Batch size	512
Learning rate warmup	Linear warmup for 10 epochs
Maximum learning rate	5×10^{-4}
Learning rate scheduler	Cosine annealing with Tmax=250 epochs
Loss function	Smooth L1
Loss ratio of energy and force	1:9
Optimizer	Adam
Exponential moving average decay	0.995
Total number of parameters	865k

We split the selected SPICE dataset into the training and validation sets using a 9:1 ratio for conformations in each molecule or system. Hyper-parameters are listed in Table S3. The models are trained parallelly on 8 NVIDIA A800 GPU cards. Training processes are carried out in a continuous way, adopting a cosine annealing learning rate scheduler until the error metrics on validation set stabilize. Upon convergence, the MAEs for energy and force settle at approximately 20 meV and 30 meV/Å, respectively.

Ablation experiment Ablation experiments are performed on the U_0 tag of QM9. We used the same training strategy described above in **QM9**. To ensure consistency in training conditions, we utilize the same dataset partitioning. Meanwhile, we have used our own implementation of PaiNN, resulting in a deviation from the initial reported MAE (5.85 eV),⁴ although this discrepancy shall not affect the comparability of ablation experiments. The results summarized in Table S4 indicate that both projection embedding and spherical harmonic expansion can improve the original performance result to some extent, while the latter is more beneficial. All training and testing in ablation experiments are carried out on a single NVIDIA RTX2080 Ti GPU card.

Table S4: Ablation experiments on the U_0 tag of QM9.

Model	MAE (meV)	Description
PaiNN	6.27	Original PaiNN
PaiNN + Projection embedding	6.21	PaiNN with auxiliary basis projection embedding
PaiNN + Spherical tensor	5.63	PaiNN with spherical tensor
XPaiNN	5.44	XPaiNN, including projection embedding and spherical tensor

Additional Results

Δ -ML results on QM9. An additional experiment has been performed, applying the Δ -ML approach using XPaiNN@xTB to four thermodynamic targets in QM9. The results are compared to those SOTA models as listed in Table S5. As is clear, the performance of XPaiNN@xTB closely matches that of the top direct-learning models, such as TensorNet⁵ and Allegro.¹² Meanwhile, OrbNet-Equi⁹(another Δ -ML model) is the best of all, which largely owes to its feature generation using quantum mechanical information as physical priors. These results suggest the promising potential of Δ -ML models.

Table S5: Test results on the thermodynamic targets in QM9 with XPaiNN@xTB, as compared to those of the other top models

Task	Unit	Allegro ^a	TensorNet ^a	OrbNet-Equi ^a	XPaiNN@xTB ^b
U_0	meV	4.7	4.3	3.5	4.38±0.08
U	meV	4.4	4.3	3.5	4.21±0.17
H	meV	4.4	4.3	3.5	4.33±0.12
G	meV	5.7	6.0	5.2	5.87±0.06

^a Results are taken from models' original publications;

^b Averaged over four models.

MD17 and rMD17. The MD17 and rMD17 datasets comprise molecular dynamics trajectories of small organic molecules. These datasets are used to assess the capability of ML models to construct potential energy surfaces (PES) with accuracy comparable to DFT calculations in their prediction of both molecular energies and atomic forces.^{13–15}

Table S6 and S7 summarize test errors in terms of MAE for various models on MD17 and rMD17, respectively. As already shown by the results on QM9, XPaiNN outperforms PaiNN in almost all tasks, while the Δ -ML models such as XPaiNN@xTB further improves over the XPaiNN. These findings may lead us to draw general conclusions regarding the suitability of equivariant GNN over invariant ones for modeling high dimensional PES. Specifically, equivariant GNNs appear to offer much improved accuracy in force prediction. Furthermore, the residual PES generated by the Δ -ML approach seems to exhibit more smoothness, making it more amenable to accurate fitting.

Table S6: Test mean absolute errors on MD17.^a

Molecule		SchNet ^b	DimeNet ^b	PaiNN ^b	NequIP ^c	Equiformer ^c	XPaiNN ^d	XPaiNN@xTB ^d
Aspirin	energy	16.0	8.8	6.9	5.7	5.3	6.6±0.2	5.5±0.0
	force	58.5	21.6	14.7	8.0	6.6	12.8±0.1	6.6±0.1
Ethanol	energy	3.5	2.8	2.7	2.2	2.2	2.4±0.1	2.2±0.0
	force	16.9	10.0	9.7	3.1	2.9	6.4±0.6	3.1±0.1
Benzene	energy	3.5	3.4	-	-	2.5	3.7±0.2	3.0±0.0
	force	13.5	8.1	-	-	8.1	6.9±0.1	6.5±0.0
Malondialdehyde	energy	5.6	4.5	3.9	3.3	3.2	3.6±0.0	3.2±0.0
	force	28.6	16.6	13.8	5.6	5.4	9.6±0.3	4.9±0.1
Naphthalene	energy	6.9	5.3	5.0	4.9	4.4	5.0±0.0	4.9±0.0
	force	25.2	9.3	3.3	1.7	2.0	3.2±0.1	1.7±0.0
Salicylic Acid	energy	8.7	5.8	4.9	4.6	4.3	4.8±0.0	4.6±0.0
	force	36.9	16.2	8.5	3.9	3.9	7.2±0.1	3.4±0.0
Toluene	energy	5.2	4.4	4.1	4.0	3.7	4.1±0.0	4.0±0.0
	force	24.7	9.4	4.1	2.0	2.1	3.5±0.1	1.9±0.0
Uracil	energy	6.1	5.0	4.5	4.5	4.3	4.5±0.0	4.5±0.0
	force	24.3	13.1	6.0	3.3	3.4	5.6±0.1	2.7±0.0

^a Unit in meV and meV/Å for energy and force, respectively, the best results are in **bold**.

^{b c} Results are taken from Ref. 4 and Ref. 2

^d Averaged over four models.

Table S7: Test mean absolute errors on rMD17. ^a

Molecule		FCHL19 ^b	NequIP ^b	Allegro ^b	XPaiNN ^c	XPaiNN@xTB ^c
Aspirin	energy	6.2	2.3	2.3	4.1±0.3	2.1±0.0
	force	20.9	8.2	7.3	13.5±0.1	6.9±0.0
Azobenzene	energy	2.8	0.7	1.2	1.7±0.2	0.7±0.0
	force	10.8	2.9	2.6	6.0±0.1	3.0±0.0
Benzene	energy	0.3	0.04	0.3	0.2±0.1	0.04±0.01
	force	2.6	0.3	0.2	0.9±0.0	0.3±0.0
Ethanol	energy	0.9	0.4	0.4	1.0±0.0	0.4±0.0
	force	6.2	2.8	2.1	6.4±0.1	2.9±0.1
Malondialdehyde	energy	1.5	0.8	0.6	1.6±0.2	0.7±0.0
	force	10.2	5.1	3.6	9.5±0.4	4.7±0.1
Naphthalene	energy	1.2	0.2	0.5	0.7±0.1	0.2±0.0
	force	6.5	1.3	0.9	2.4±1.6	1.3±0.0
Paracetamol	energy	2.9	1.4	1.5	2.4±0.1	1.2±0.0
	force	12.2	5.9	4.9	9.6±0.2	4.9±0.0
Salicylic Acid	energy	1.8	0.7	0.9	1.4±0.0	0.6±0.0
	force	9.5	4.0	2.9	7.5±0.1	3.5±0.1
Toluene	energy	1.6	0.3	0.4	0.7±0.1	0.2±0.0
	force	8.8	1.6	1.8	3.5±0.1	1.4±0.0
Uracil	energy	0.6	0.4	0.6	0.8±0.0	0.4±0.0
	force	4.2	3.1	1.8	5.6±0.1	2.5±0.0

^a Unit in meV and meV/Å for energy and force respectively, best results in **bold** except for Δ -ML models.

^b Results are taken from Ref. 12

^c Averaged over four models.

Additional subsets in GMTKN55. It is of great interest to take a further look on the performances of our models on chemical diverging systems such as charged, open-shell molecules as well as species containing untrained elements, as our training dataset does not involve these systems. For this purpose, we have selected additional subsets from GMTKN55 that contain charged, open-shell molecules as well as unseen elements to form three subsets, which complement our original benchmark. The description of the chosen subsets can be found in Table S8, and detailed results are provided in Table S9. It is worth noting that, AIQM1 model does not support this additional test due to the limitation on element types.

As can be seen, for subsets containing charged or open-shell species, direct learning model XPaiNN performs poorly due to its inability to accurately distinguish the complexities of electronic structures. On the other hand, Δ -ML model XPaiNN@xTB continues to offer much improved descriptions on these systems, such as RSE43, WATER27 and IL6. This superiority shall largely be attributed to the integration of the SQM method. Performances are close between XPaiNN@xTB and OrbNet-Equi in the first two selected collections in Table S9. A better result of OrbNet-Equi in the third collection can be understood as its training set covers a wider range of chemical elements than our XPaiNN. For example, Si that presents in ICONF is known to OrbNet-Equi. The same is true for B exists in various small molecules involved in reactions in NBPRC and G2RC.

All in all, our findings here reinforce the opinions in our main text that an enhanced transferability is achieved via the Δ -ML approach in describing the chemically diverging systems. Moreover, these results highlight the necessity of encompassing a broad chemical space for constructing atomistic ML model of general purpose, where data-efficiency is of critical concern.

Table S8: Description of benchmark subset in GMTKN55 database.

Subset	Description
	Basic properties and reaction energies for small systems
AL2X6 ^d	Dimerization energies of AlX ₃ compounds
NBPRC ^d	Oligomerizations and H ₂ fragmentations of NH ₃ /BH ₃ systems H ₂ activation reactions with PH ₃ /BH ₃ systems
ALK8 ^b	Dissociation and other reactions of alkaline compounds
RC21 ^c	Fragmentations and rearrangements in radical cations
G2RC ^d	Reaction energies of selected G2/97 systems
BH76RC ^c	Reaction energies of the BH76 set
FH51 ^a	Reaction energies in various (in-)organic systems
TAUT15 ^a	Relative energies in tautomers
	Reaction energies for large systems and isomerization reactions
DARC ^a	Reaction energies of Diels-Alder reactions
RSE43 ^c	Radical-stabilization energies
BSR36 ^a	Bond-separation reactions of saturated hydrocarbons
CDIE20 ^a	Double-bond isomerization energies in cyclic systems
ISO34 ^a	Isomerization energies of small- and medium-sized organic molecules
C60ISO ^a	Relative energies between C ₆₀ isomers
PArel ^b	Relative energies in protonated isomers
	Reaction barrier heights
BH76 ^c	Barrier heights of hydrogen transfer, heavy atom transfer, nucleophilic substitution, unimolecular, and association reactions
BHPERI ^d	Barrier heights of pericyclic reactions
BHDIV10 ^d	Diverse reaction barrier heights
BHROT27 ^a	Barrier heights for rotation around single bonds
PX13 ^a	Proton-exchange barriers in H ₂ O, NH ₃ , and HF clusters
WCPT18 ^a	Proton-transfer barriers in uncatalyzed and water-catalyzed reactions
	Intermolecular noncovalent interactions
ADIM6 ^a	Interaction energies of n-alkane dimers
S22 ^a	Binding energies of noncovalently bound dimers
S66 ^a	Binding energies of noncovalently bound dimers

^a Subsets consist of neutral and closed-shell molecules.

^b Subsets contain charged but closed-shell molecules.

^c Subsets contain charged and open-shell molecules.

^d Subsets of uncharged and closed-shell molecules, but involve unknown elements.

Subset	Description
HEAVY28 ^d	Noncovalent interaction energies between heavy element hydrides
WATER27 ^b	Binding energies in (H ₂ O) _n , H ⁺ (H ₂ O) _n , and OH ⁻ (H ₂ O) _n
CARBHB12 ^d	Hydrogen-bonded complexes between carbene analogues and H ₂ O, NH ₃ , or HCl
PNICO23 ^d	Interaction energies in pnictogen-containing dimers
HAL59 ^a	Binding energies in halogenated dimers (incl. halogen bonds)
AHB21 ^b	Interaction energies in anion-neutral dimers
CHB6 ^b	Interaction energies in cation-neutral dimers
IL16 ^b	Interaction energies in anion-cation dimers
Intramolecular noncovalent interactions	
IDISP ^a	Intramolecular dispersion interactions
ICONF ^d	Relative energies in conformers of inorganic systems
ACONF ^a	Relative energies of alkane conformers
Amino20x4 ^a	Relative energies in amino acid conformers
PCONF21 ^a	Relative energies in tri- and tetrapeptide conformers
MCONF ^a	Relative energies in melatonin conformers
SCONF ^a	Relative energies of sugar conformers
UPU23 ^b	Relative energies between RNA-backbone conformers
BUT14DIOL ^a	Relative energies in butane-1,4-diol conformers

^a Subsets consist of neutral and closed-shell molecules.

^b Subsets contain charged but closed-shell molecules.

^c Subsets contain charged and open-shell molecules.

^d Subsets of uncharged and closed-shell molecules, but involve unknown elements.

Table S9: WTMAD-2 for additional subsets in GMTKN55. Unit in kcal/mol.

Subset	ω B97M-D3(BJ)	GFN2-xTB	GFN-xTB	OrbNet-Equi	XPaiNN	XPaiNN@xTB
Basic properties and reaction energies for small systems						
AL2X6 ^d	3.35	23.17	24.04	20.13	138.61	96.94
NBPRC ^d	2.88	21.55	22.48	23.78	64.77	30.73
ALK8 ^b	2.57	21.71	47.71	68.22	72.57	30.06
RC21 ^c	2.29	37.68	35.10	36.22	56.70	33.80
G2RC ^d	2.32	24.31	32.46	16.20	27.75	31.96
BH76RC ^c	2.11	49.19	56.17	45.99	50.26	54.51
Reaction energies for large systems and isomerization reactions						
RSE43 ^c	5.64	56.92	50.68	44.20	49.31	26.83
PArel ^b	7.78	71.97	55.78	43.37	91.87	75.47
Reaction barrier heights						
BH76 ^c	3.85	59.86	64.16	56.99	45.79	53.94
BHPERI ^d	3.31	27.87	25.38	10.54	72.92	16.05
BHDIV10 ^d	1.49	10.18	10.54	8.15	17.42	10.39
HEAVY28 ^d	12.38	27.83	29.96	54.33	60.46	42.59
Intermolecular noncovalent interactions						
WATER27 ^b	0.35	2.14	5.18	12.03	20.15	1.86
CARBHB12 ^d	2.05	16.89	6.32	19.69	16.89	20.92
PNICO23 ^d	3.42	14.70	31.02	39.03	95.09	72.55
AHB21 ^b	1.12	7.51	11.83	18.59	46.36	15.20
CHB6 ^b	1.94	11.47	8.37	23.97	90.08	13.31
IL16 ^b	0.58	2.25	2.97	2.55	31.79	3.08
Intramolecular noncovalent interactions						
ICONF ^d	3.06	28.35	45.73	29.76	65.08	51.39
UPU23 ^b	6.25	28.87	12.31	10.99	17.81	18.10
WTMAD-2 <i>b</i>	3.09	21.47	18.73	21.20	44.58	22.02
WTMAD-2 <i>c</i>	3.81	54.49	55.75	49.25	48.82	44.69
WTMAD-2 <i>d</i>	4.50	22.85	27.65	27.22	60.14	39.35

^b Subsets contain charged but closed-shell molecules.

^c Subsets contain charged and open-shell molecules.

^d Subsets contain uncharged and closed-shell molecules, but involve unknown elements.

ROT34. Table S10 summarizes the RMSD for each molecule between reference structures and the optimized structures sourced by different methods. Optimized structures of GFN-xTB, GFN2-xTB, ANI-2x and OrbNet-Equi are obtained from Ref. 9, while the others can be found in the attached zip file. RMSDs are calculated using the quaternions method.¹⁶

Table S10: RMSD of different methods for each molecule in ROT34. Unit in Å

Compound	ω B97M-D3(BJ)	GFN-xTB	GFN2-xTB	ANI-2x	OrbNet-Equi	XPaiNN	XPaiNN@xTB
Ethynyl-cyclohexane	0.006	0.012	0.016	0.015	0.011	0.008	0.011
Isoamyl-acetate	0.035	0.692	0.500	0.069	0.141	0.058	0.053
Diisopropylketone	0.015	0.057	0.043	0.062	0.020	0.052	0.059
Bicyclo[2.2.2]octadiene	0.005	0.031	0.029	0.035	0.013	0.026	0.016
Triethylamine	0.021	0.119	0.138	0.071	0.013	0.055	0.055
Vitamin C	0.016	0.073	0.071	0.143	0.054	0.058	0.028
Serotonin	0.024	0.031	0.053	0.077	0.036	0.018	0.026
Aspirin	0.072	0.126	0.192	0.229	0.037	0.118	0.112
Cassyrane	0.012	0.096	0.084	0.289	0.059	0.075	0.038
Limonene	0.020	0.075	0.029	0.031	0.031	0.015	0.023
Lupinine	0.011	0.054	0.046	0.033	0.038	0.026	0.020
Proline derivative	0.016	0.097	0.038	0.070	0.026	0.033	0.031
Average	0.021	0.122	0.103	0.094	0.040	0.045	0.039

Computation Efficiency. To compare method efficiency, we document the time consumption of methods used for calculating the reaction enthalpy of reaction **a** in Fig.4 in the main text. The results are listed in Table S11. As can be seen, our model is significantly faster than the DFT method while maintaining a close accuracy.

Table S11: CPU time for reaction **a**. calculated by different methods. Unit in second.

Reaction	ω B97M-D3(BJ)	GFN2-xTB	XPaiNN	XPaiNN@xTB
Total CPU Time	3.20×10^5	15.6	107	109

Detailed results for the **S66x8**, **Torsion**, and **BH9** datasets are provided in the attached zip file.

References

- (1) Geiger, M.; Smidt, T. e3nn: Euclidean Neural Networks. *arXiv [Preprint]* **2022**, <https://arxiv.org/abs/2207.09453>.
- (2) Liao, Y.-L.; Smidt, T. Equiformer: Equivariant graph attention transformer for 3D atomistic graphs. *arXiv [Preprint]* **2023**, <https://doi.org/10.48550/arXiv.2206.11990>.
- (3) Unke, O. T.; Bogojeski, M.; Gastegger, M.; Geiger, M.; Smidt, T.; Müller, K.-R. SE(3)-equivariant prediction of molecular wavefunctions and electronic densities. *arXiv [Preprint]* **2021**, <https://arxiv.org/abs/2106.02347>.
- (4) Schütt, K.; Unke, O.; Gastegger, M. Equivariant message passing for the prediction of tensorial properties and molecular spectra. *arXiv [Preprint]* **2021**, <https://arxiv.org/abs/2102.03150>.
- (5) Simeon, G.; Fabritiis, G. D. TensorNet: Cartesian Tensor Representations for Efficient Learning of Molecular Potentials. *arXiv [Preprint]* **2023**, <https://doi.org/10.48550/arXiv.2306.06482>.
- (6) Smith, J. S.; Isayev, O.; Roitberg, A. E. ANI-1: an extensible neural network potential with DFT accuracy at force field computational cost. *Chem. Sci.* **2017**, *8*, 3192–3203.
- (7) Devereux, C.; Smith, J. S.; Huddleston, K. K.; Barros, K.; Zubatyuk, R.; Isayev, O.; Roitberg, A. E. Extending the applicability of the ANI deep learning molecular potential to sulfur and halogens. *J. Chem. Theory Comput.* **2020**, *16*, 4192–4202.
- (8) Qiao, Z.; Welborn, M.; Anandkumar, A.; Manby, F. R.; Miller III, T. F. OrbNet: Deep learning for quantum chemistry using symmetry-adapted atomic-orbital features. *J. Chem. Phys.* **2020**, *153*, 124111.

- (9) Qiao, Z.; Christensen, A. S.; Welborn, M.; Manby, F. R.; Anandkumar, A.; Miller, T. F. Informing geometric deep learning with electronic interactions to accelerate quantum chemistry. *Proc. Natl. Acad. Sci. U. S. A.* **2022**, *119*, e2205221119.
- (10) Bannwarth, C.; Ehlert, S.; Grimme, S. GFN2-xTB—An accurate and broadly parametrized self-consistent tight-binding quantum chemical method with multipole electrostatics and density-dependent dispersion contributions. *J. Chem. Theory Comput.* **2019**, *15*, 1652–1671.
- (11) Gasteiger, J.; Groß, J.; Günnemann, S. Directional message passing for molecular graphs. ICLR. 2020.
- (12) Musaelian, A.; Batzner, S.; Johansson, A.; Sun, L.; Owen, C. J.; Kornbluth, M.; Kozinsky, B. Learning local equivariant representations for large-scale atomistic dynamics. *Nat. Commun.* **2023**, *14*, 579.
- (13) Chmiela, S.; Tkatchenko, A.; Sauceda, H. E.; Poltavsky, I.; Schütt, K. T.; Müller, K.-R. Machine learning of accurate energy-conserving molecular force fields. *Sci. Adv.* **2017**, *3*, e1603015.
- (14) Chmiela, S.; Sauceda, H. E.; Müller, K.-R.; Tkatchenko, A. Towards exact molecular dynamics simulations with machine-learned force fields. *Nat. Commun.* **2018**, *9*, 3887.
- (15) Christensen, A. S.; von Lilienfeld, O. A. On the role of gradients for machine learning of molecular energies and forces. *Mach. Learn.: Sci. Technol.* **2020**, *1*, 045018.
- (16) Coutsiias, E. A.; Seok, C.; Dill, K. A. Using quaternions to calculate RMSD. *J. Comput. Chem.* **2004**, *25*, 1849–1857.